Journal of Building Engineering 44 (2021) 102884

Contents lists available at ScienceDirect

Journal of Building Engineering

journal homepage: www.elsevier.com/locate/jobe

New moment-resisting beam-column joints to increase progressive collapse resistance of precast concrete buildings

Hussein M. Elsanadedy [1]

Chair of Research and Studies in Strengthening and Rehabilitation of Structures, Dept. of Civil Eng., College of Eng., King Saud University, P.O. Box 800, Riyadh, 11421, Saudi Arabia

ARTICLE INFO

Keywords:
Progressive collapse
Precast beam-column connection
Monolithic beam-column connection
Column-removal scenario
Finite element model

ABSTRACT

Since existing precast RC (reinforced concrete) structures are lacking structural continuity at regions of beam-column connections, they are less resistant to progressive collapse in the event of column removal than CIS (cast-in-situ) RC structures. The prime objectives of current research are to revise the existing precast simple shear beam-column connections and to develop new precast moment connections for increasing the progressive collapse robustness of precast buildings. To achieve these goals, 11 half-scale beam-column assemblies – comprising two beams and three columns – were numerically investigated under the middle column removal scenario using nonlinear 3D FE (finite element) modeling. Two specimens represented typical existing precast simple beam-column connections, and three specimens had revised precast simple connections. Four assemblies were designed with new precast moment connections. The last two specimens represented CIS concrete beam-column connections with continuous and discontinuous longitudinal beam bars to be compared with the precast assemblies. The FE modeling incorporated strain rate-dependent nonlinear constitutive models, contact between different parts in the connection region, and bond-slip at steel bars-to-concrete interface. As a key outcome of this research, the newly developed precast moment connection with the highest rotational ductility was recommended for diminishing the potential of progressive collapse in precast concrete buildings.

1. Introduction

Due to their numerous advantages such as efficient construction cost (owing to minimum use of formwork and skilled labor), speed of construction, high quality control of materials, and minimum construction waste, precast RC structures have widely spread all over the globe. Generally, structures are vulnerable to progressive collapse in case of losing one or more load-carrying members (such as columns) owing to extreme events such as blast loads, impact, seismic waves, or fire. As it may lead to causalities in terms of loss of human lives and/or property, the risk of progressive collapse has to be mitigated (or minimized) in structures. Since existing precast RC structures are lacking structural continuity at regions of beam-column connections, they are less resistant to progressive collapse – in the event of column removal – than monolithically cast RC structures. The behavior of precast RC systems depends mainly on the performance of their joints, particularly between columns and beams. Detailing of precast RC beam-column connections affects the structural performance of building frames in terms of strength and ductility. Fig. 1 shows examples of typical precast beam-column connections used in buildings constructed in Saudi Arabia.

Several studies investigated the performance of various details of monolithic and precast beam-column joints [1–7]. For precast concrete joints, these incorporated: (a) connections using dowel bars with or without steel cleat angles (with or without stiffeners); (b) connections with steel plates and tie rods; (c) utilizing cast-in-situ (CIS) concrete in the joint region; and (d) utilizing bolted connections, etc.

Hawileh et al. [8] used the FE method to investigate the cyclic behavior of a precast hybrid beam-column joint, which was tested previously by Cheok and Stone at NIST [9]. The FE model considered material nonlinearity, pre-tension effect in the post-tensioning strands, and surface-to-surface contact between different parts. The numerical modeling matched well with the test results and observations. The study recommended that the developed model can be utilized in forthcoming studies to investigate the impact of different parameters such as material properties, boundary conditions, location of the post-tensioning strands, and duct grouting. In another study, Kaya and Arslan [10] examined experimentally and numerically the seismic behavior of post-tensioned precast beam-column joints. One monolithic and three precast

E-mail address: helsanadedy@ksu.edu.sa.
[1] On leave from Helwan Univ., Cairo, Egypt.

Available online 17 June 2021
2352-7102/
Received 5 January 2021; Received in revised form 2 June 2021; Accepted 11 June 2021

beam-column joints were tested under cyclic loading. The tested specimens were also simulated using the FE method to assess their load-displacement response. The results of the experimental and FE analysis showed that the behavior of the post-tensioned precast connections was adequate concerning load-carrying capacity.

Cai et al. [11] studied experimentally and numerically the seismic performance of a new type of self-centering post-tensioned precast beam-column joint, assembled via unbonded post-tensioning strands and top and seat steel angles. The tests included eight beam-column assemblies with varying parameters. The results indicated that the properly designed assemblies had good re-centering capacity and high initial stiffness and ductility. In another study, Ding et al. [12] developed new precast concrete bolted beam-column connections for seismic resistance. Full-scale tests were performed on two connections with grade 5.6 and 8.8 bolts, respectively. The proposed connections were found to have excellent performance in resisting the seismic loading. Hwang et al. [13] tested post-tensioned precast beam-column joints under fully reversed cyclic loading. The investigated parameters incorporated grout strength at the beam-to-column interface and level of prestressing stress in the post-tensioning strands. The experimental results identified that the post-tensioned precast concrete beam-column joints had a seismic performance equal to that of conventional RC beam-column connections.

The vulnerability of structures to progressive collapse can be assessed by studying the impact of abrupt removal of column(s) on load redistribution and the development of alternate load paths. Several studies are available in the literature on the progressive collapse potential of framed buildings [14–31]. For example, Sasani et al. [25] studied numerically the progressive collapse potential of a 10-story concrete building owing to the loss of the outer column as a consequence of blast loading. The building could resist progressive collapse owing to redistributing the loads. Yu and Tan [26] studied the impact of seismic detailing on the behavior of CIS concrete beam-column joints in the event of column removal. They tested two half-scale CIS concrete beam-column assemblies, which were detailed as per the non-seismic and seismic codes. In another research, Li and Sasani [27] investigated the effect of seismic design and detailing on the vulnerability of CIS concrete frames in multistory buildings to progressive collapse under column-loss events. Wang et al. [28] tested CIS concrete assemblies having specially shaped columns under column-loss scenarios for assessing their robustness to progressive collapse. The redistribution of internal forces relied mainly on the beam-resisting mechanism, and the compression arch action developed in the beams enhanced the progressive collapse resistance.

Kang and Tan [29] tested precast concrete beam-column frames under the loss of a column. Details of the beam-column connections involved CIS concrete layer over beams and joints, top continuous beam bars through the joint, 90° bend, and lap splicing of beam bars at the middle joint. The center column of the frame assembly was subjected to quasi-static loading. The test results identified that the use of CIS top concrete layer over beams and joints along with continuous beam bars helped in the formation of both compression arch and catenary action phases. Kang et al. [30] tested precast concrete beam-column assemblies in the event of column loss. Details of beam-column connections included the use of cementitious composites in the CIS top concrete layer. It was concluded that the formation of both compression arch and catenary actions was in sequence with the increase in the middle column displacement. In another research, Nimse et al. [31] tested precast concrete beam-column frames under the removal of the middle column. Assemblies with CIS concrete joints were also investigated for comparison. Different detailing of precast joints was studied. The performance of test assemblies was compared with regard to their load-displacement response.

In a study by Morone and Sezen [32], an existing 4-story RC building – having flat slabs with drop panels and scheduled for demolition – was instrumented and tested by sequentially removing three columns of the first story to investigate its collapse behavior. During the removal of each column, redistribution of loads to the neighboring columns was recorded. Based on the test data obtained from the building experiment, a simplified model was developed for quick progressive collapse assessment of multi-story buildings.

An experimental program was conducted at NIST by Main et al. [33] to examine the progressive collapse risk of precast concrete moment-frame joints. Two full-scale precast assemblies were tested under the middle column loss event. They simulated part of the outer ordinary and special precast moment frames, respectively, of 10-story buildings. Each assembly consisted of a spandrel beam connected to precast columns. The moment connections comprised two link plates welded to both steel plates embedded in the column and steel angles embedded in the beam. The yield capacity was not reached for the two assemblies and they failed in a brittle mode owing to premature fracture of the welded anchorage bars at relatively small beam chord rotations. In another study, Quiel et al. [34] developed a new moment connection for progressive collapse resistance in precast concrete building frames. The connection used unbonded high-strength steel post-tensioning bars that passed through ducts in the column and were anchored to the beams via bearing plates. A full-scale quasi-static pushdown test was carried out on two designs of the suggested connection: one with higher moment resistance and limited ductility, and the other one with lower flexural resistance and higher ductility. The developed connection attained its design yield capacity, had good performance under service level demands, and achieved moderate to high ductility.

In a recent study, Zhou et al. [35] tested two half-scale concrete beam-column specimens including one monolithic and one precast to assess their progressive collapse risk under the loss of the middle column. In the precast specimen, dowel bars embedded in the corbel, steel cleat angles, U-shaped bars, and horizontal hoops were utilized in the beam-column joint region. The progressive collapse capacity of the precast specimen was about 77% of the monolithic specimen. The compressive arch action was pronounced in both assemblies; however,

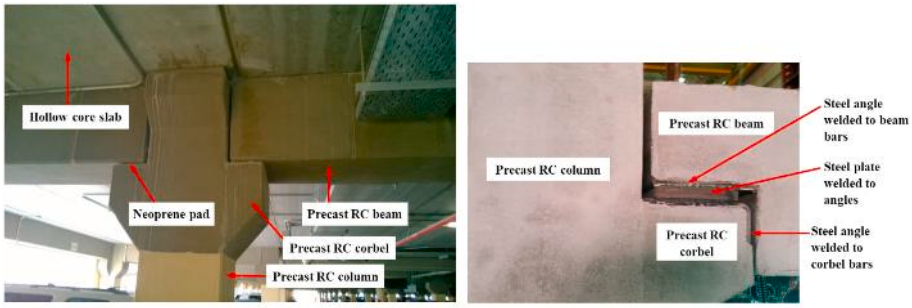

Fig. 1. Commonly used precast concrete beam-column joints: (a) Type 1; (b) Type 2.

the catenary action phase was formed in the monolithic specimen only.

An experimental study was completed at King Saud University to examine the progressive collapse resistance of precast concrete beam-column assemblies having two types of simple shear connections under the loss of middle column [36,37]. Precast assemblies simulated the most commonly used types of beam-column joints in precast construction within Saudi Arabia (see Fig. 1). Two monolithic specimens – one having continuous main beam bars and the other one having discontinuous bottom beam bars – were utilized for comparison. The performance of all specimens was compared concerning their load-displacement response.

The goals of this study are to revise the existing precast simple shear beam-column connections and to develop new precast moment-resisting connections for increasing the progressive collapse robustness of precast buildings. In this regard, 11 beam-column assemblies were numerically investigated under the removal of the middle column using FE modeling. The specimens included two assemblies with typical existing precast simple shear connections, three assemblies with revised precast simple shear connections, four assemblies with new precast moment connections, and two monolithic specimens – with and without continuous beam bars – for comparison with the precast assemblies. The FE modeling incorporated strain rate-dependent nonlinear constitutive models, contact between different parts in the connection region, and bond-slip at the interface of steel bars with the surrounding concrete. The FE models of the two precast assemblies with typical existing simple shear connections and the monolithic specimen with continuous beam bars were validated in a previous study by Elsanadedy et al. [38] using the test results available in Ref. [36]. However, the FE model of the monolithic specimen with discontinuous beam bars was validated in this study using the test results detailed in Ref. [37]. The performance of different specimens was compared with regard to failure mode and load-displacement response.

2. Analysis matrix

For accomplishing the research objectives, 11 beam-column assemblies – comprising two beams and three columns of a single story – were numerically investigated under the loss of the middle column using nonlinear 3D FE modeling. Table 1 presents details of the FE analysis matrix, which included 9 precast non-prestressed specimens and two monolithic frames. The precast assemblies – with regard to dimensions and details of reinforcing steel – were selected as half-scale of a prototype exterior frame that was extracted from an existing precast concrete building. It is worth mentioning that in the designation of assemblies in Table 1, the letters "P" and "M" stand for precast and monolithic specimens, respectively; the symbols "SC" and "MC" signify simple shear and moment connections, respectively; the acronyms "T1" and "T2" denote types 1 and 2 precast connections, respectively; the symbol "NP" means neoprene pad; and the acronyms "ANG" and "PB_ANG" stand for attached and perfectly bonded steel angles, respectively. As identified in Table 1, the studied specimens are categorized into three main groups, which are detailed in the following subsections.

2.1. Precast specimens with type 1 connections

In this group, 5 precast assemblies with type 1 of beam-column connections were studied (see Fig. 1(a)). This group was divided into three precast assemblies with simple shear beam-column connections (P-SC-T1-NP, P–SC–T1-ANG, and P–SC–T1-PB_ANG) and two precast specimens having moment connections (P-MC-T1-ANG and P-MC-T1-PB_ANG).

2.1.1. Simple shear connections

The first specimen (P-SC-T1-NP) represented type 1 of the typical precast RC beam-column joints utilized in structures constructed in Saudi Arabia. The concrete dimensions and details of steel

Table 1
Details of FE analysis matrix.

Assembly ID	Type of beam-column connection	Details of beam-column connection	Comments
Precast specimens with type 1 connections			
P–SC–T1-NP	Simple	• End of precast beam was supported by neoprene pad resting on the corbel (Fig. 2). • 1ϕ16 mm steel bar was monolithically cast with the corbel and grouted with the precast beam using cementitious mortar (Fig. 2).	• Control specimen • Tested in Refs. [36,37]
P–SC–T1-ANG	Simple	Same as P–SC–T1-NP but the neoprene pads were replaced with steel plates that were welded to two pre-installed angles: one tied to the end of the precast beam and the other one tied to the top side of the corbel before concrete casting (Fig. 4).	New connection
P–SC–T1-PB_ANG	Simple	Same as P–SC–T1-ANG but with assuming perfect bond at the concrete-to-steel angles interface.	New connection
P-MC-T1-ANG	Moment	Same as P–SC–T1-ANG, but with the following: (1) The top 90 mm thickness of the beam was made of CIS concrete for a distance of 1130 mm at both ends; (2) the top beam bars were continuous at the joint; and (3) the gap at the interface of beam with column was filled with cementitious mortar (Fig. 6).	New connection
P-MC-T1-PB_ANG	Moment	Same as P-MC-T1-ANG but with assuming perfect bond at the concrete-to-steel angles interface.	New connection
Precast specimens with type 2 connections			
P–SC–T2-ANG	Simple	• End of precast beam was supported by steel plate welded to two pre-installed angles: one tied to the end of the precast beam and the other one tied to the top side of the corbel before concrete casting (Fig. 7). • 1ϕ16 mm steel bar was monolithically cast with the corbel and grouted with the precast beam using cementitious mortar (Fig. 7).	• Control specimen • Tested in Ref. [36]
P–SC–T2-PB_ANG	Simple	Same as P–SC–T2-ANG but with assuming perfect bond at the concrete-to-steel angles interface.	New connection
P-MC-T2-ANG	Moment	Same as P–SC–T2-ANG, but with the following: (1) The top 90 mm thickness of the beam was made of CIS concrete for a distance of 1130 mm at both ends; (2) the top beam bars were continuous at the joint; and (3) the gap at the interface of beam with column was filled with cementitious mortar (Fig. 8).	New connection
P-MC-T2-PB_ANG	Moment	Same as P-MC-T2-ANG but with assuming perfect bond at the concrete-to-steel angles interface.	New connection
Monolithic specimens			

(continued on next page)

Table 1 (*continued*)

Assembly ID	Type of beam-column connection	Details of beam-column connection	Comments
M-CBR	Monolithic	Monolithic with continuous bottom and top beam bars (Fig. 9).	• Control specimen • Tested in Refs. [36,37]
M-DBR	Monolithic	Monolithic, where the top beam bars were continuous through the connection; however, the bottom bars were discontinuous (Fig. 9).	• Control specimen • Tested in Ref. [37]

reinforcement of this specimen are shown in Fig. 2. It should be noted that this specimen was previously tested in the event of middle column loss [36,37]. For beams and columns, section dimensions of 350 × 350 mm were utilized; however, the section size of the corbels was 350 × 250 mm (see Fig. 2). The column height measured to the bottom of the precast beam was 1050 mm, and the column rested on a steel I-shaped stub of height 500 mm making the total clear height of the precast assembly 1550 mm (see Fig. 3). The steel stubs were then attached to steel rails tied to the lab floor (Fig. 3). It is worth noting that the steel stubs, attached to the lower part of the precast columns, were designed so that their flexural stiffness is nearly the same as that for the precast RC columns [36,37]. Beams were supported by neoprene pads resting on the

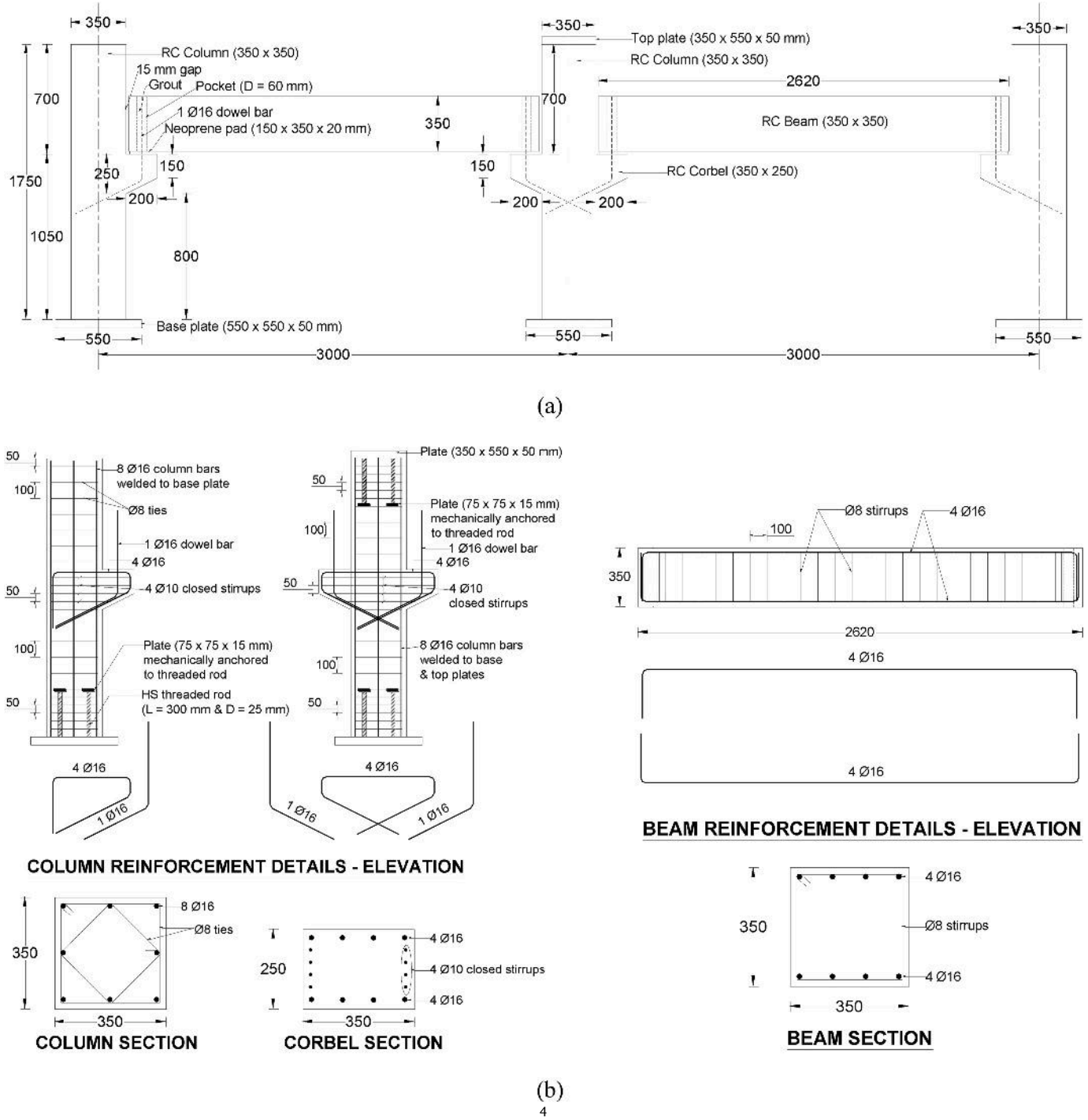

Fig. 2. Details of precast assembly P–SC–T1-NP [36,37] (Dimensions are measured in mm): (a) Concrete dimensions; (b) Reinforcement.

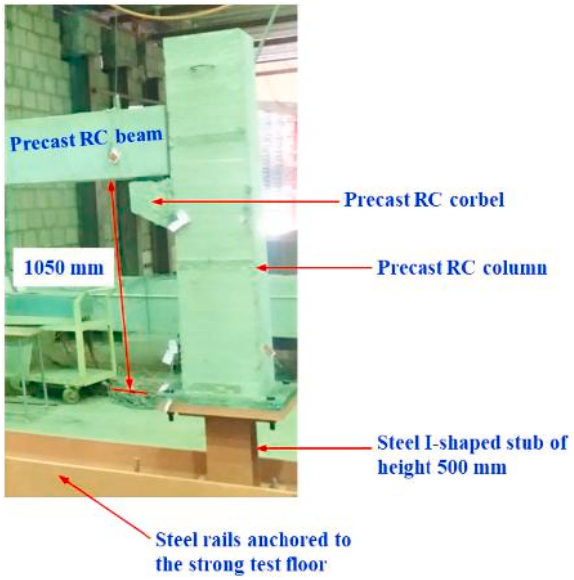

Fig. 3. Support for the outer column of assembly P–SC–T1-NP [36,37].

RC corbel. The beam-column joints consisted of 1ϕ16 mm steel bar that was monolithically cast with the corbel and grouted with the precast beam using non-shrink cementitious mortar (see Fig. 2).

The second specimen P–SC–T1-ANG was a revised version of assembly P–SC–T1-NP, and this revision was suggested in this study to enhance its progressive collapse resistance under the middle column loss event. As noted from Table 1, the beam-column connection of assembly P–SC–T1-ANG was taken to be similar to that of P–SC–T2-ANG, which was previously tested under the middle column loss scenario [36]. Specimen P–SC–T1-ANG is the same as P–SC–T1-NP; however, the neoprene pads were replaced with steel plates that were welded to two pre-installed angles: one tied to the end of the precast beam and the other one tied to the top side of the corbel before concrete casting (see Fig. 4). These angles were spot welded to the main reinforcement of the beam and corbel.

As discussed in Ref. [36], failure of specimen P–SC–T2-ANG (having beam-column joint like that of assembly P–SC–T1-ANG) was owing to debonding at the interface of corbel with angle. Accordingly, another revision has been suggested in the current study for improving the performance of the beam-column connection of specimen P–SC–T1-ANG under the middle column removal scenario. In this revision, special care has been given to the anchorage of steel angles inside the concrete of the beam and corbel. In this regard, specimen P–SC–T1-PB_ANG has been suggested in which full anchorage was assumed at the interface of angles with concrete of the beam and corbel. In reality, this proper anchorage could be obtained via mechanical means; e.g. use of high-strength headed shear studs welded to the angle and affixed into the beam (or corbel) before concrete casting (see Fig. 5). As will be detailed later, this full anchorage was modeled by the assumption of a perfect bond at the interface of angles with concrete.

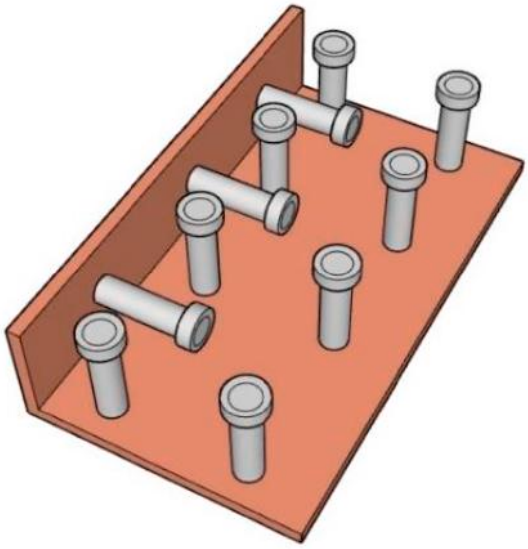

Fig. 5. Proposed idea for fully anchoring the angles with precast beams and corbels of assemblies P–SC–T1-PB_ANG, P-MC-T1-PB_ANG, P–SC–T2-PB_ANG, and P-MC-T2-PB_ANG.

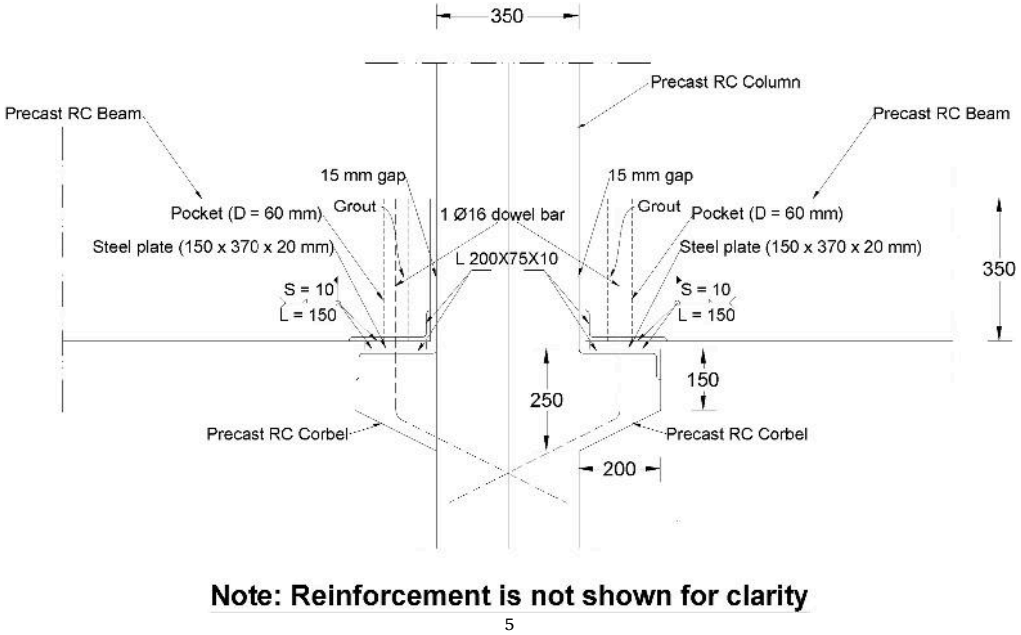

Fig. 4. Details of middle connection for precast assembly P–SC–T1-ANG (Dimensions are measured in mm).

2.1.2. Moment connections

In addition to the three precast specimens with type 1 simple shear connections, two precast assemblies with new type 1 moment connections were numerically investigated as depicted in Table 1. The first specimen P-MC-T1-ANG was the same as P–SC–T1-ANG, but with wet/dry beam/column joint with continuous top beam bars. Details of precast assembly P-MC-T1-ANG with the proposed type 1 moment connection are given in Fig. 6. In this assembly, the top 90 mm thickness of the beam was made of CIS concrete for a distance of 1130 mm at both ends. The top beam bars were made continuous through the connection using high strength couplers tied at the end of beam bars that were pre-constructed with the precast columns as presented in Fig. 6. These couplers were used for mechanical splicing of the top bars of the beam in the wet connection zone. As shown in Fig. 6, these bars, in turn, were lap spliced with the pre-constructed top bars of the precast beam using class B tension splice as per the ACI 318–19 code [39] (= 1130 mm for ϕ16 mm bars). The gap at the interface of the beam with the column was filled with non-shrink cementitious mortar (see Fig. 6). The second assembly with type 1 moment connection (P-MC-T1-PB_ANG) is the same as P-MC-T1-ANG but with full anchorage at the interface of angles with

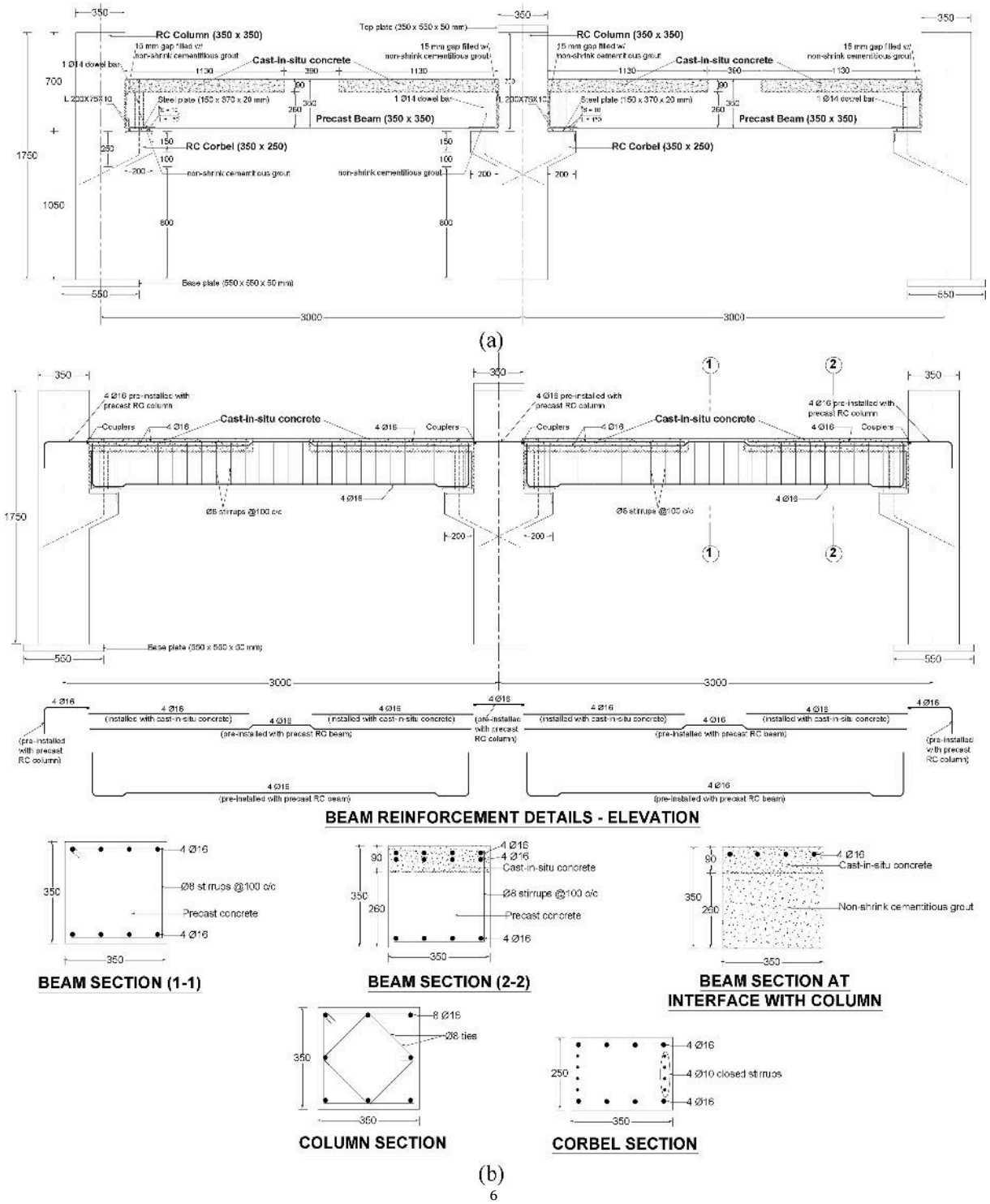

Fig. 6. Details of precast assembly P-MC-T1-ANG with type 1 moment connection (Dimensions are measured in mm): (a) Concrete dimensions; (b) Reinforcement.

concrete of the beam and corbel. This has been achieved in the FE modeling by the assumption of a perfect bond at the interface.

2.2. Precast specimens with type 2 connections

Investigated in this group were four precast frames with type 2 of beam-column connections (see Fig. 1(b)). The specimens included two precast assemblies with simple shear beam-column connections (P-SC-T2-ANG and P–SC–T2-PB_ANG), and two precast frames with moment connections (P-MC-T2-ANG and P-MC-T2-PB_ANG).

2.2.1. Simple shear connections

The first assembly (P-SC-T2-ANG) represented type 2 of the typical precast RC beam-column joints utilized in structures constructed in Saudi Arabia. Fig. 7 presents the dimensions and details of assembly P–SC–T2-ANG. Similar to P–SC–T1-NP, this specimen was previously tested under the middle column loss scenario [36]. As seen from Fig. 7, the dimensions and detailing of specimen P–SC–T2-ANG were almost similar to the control specimen P–SC–T1-NP, except that the precast beams had dapped end with a reduced section of 350 × 180 mm for a distance of 200 mm at both ends. Instead of the neoprene pads, beams of specimen P–SC–T2-ANG rested on a steel plate of 20 mm thickness. The plate was welded to two pre-installed steel angles as shown in Fig. 7. One angle was affixed to the top side of the RC corbel, whereas the other one was attached to the bottom side of the dapped beam end before casting of concrete. The angles were spot welded to the main reinforcement of the beam and corbel. Besides the angles-to-plate assembly at end of precast beams, 1ϕ16 mm bar was monolithically cast with the corbel and grouted with the precast beam using non-shrink cementitious mortar (see Fig. 7).

As per the test results of control specimen P–SC–T2-ANG, discussed previously in Ref. [36], failure was owing to debonding at the interface of corbel with angle. Hence, revision of this assembly has been proposed in the current study for enhancing its performance under the middle column loss scenario. Special attention has been given to the anchorage of steel angles with the concrete of beam and corbel. Therefore, specimen P–SC–T2-PB_ANG has been suggested in which full anchorage was assumed at the interface of angles with concrete. As mentioned

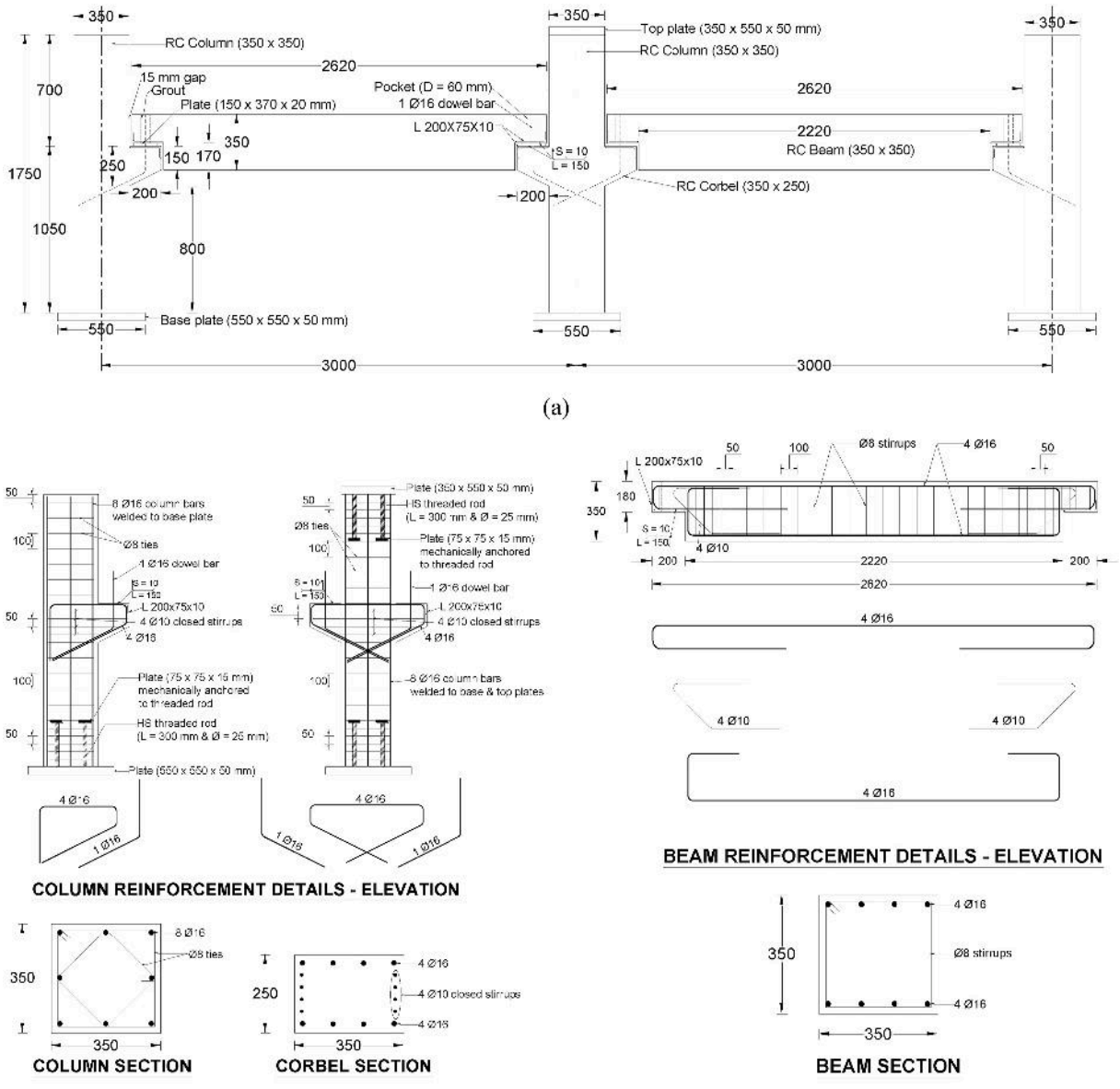

Fig. 7. Details of precast assembly P–SC–T2-ANG [36] (Dimensions are measured in mm): (a) Concrete dimensions; (b) Reinforcement.

previously, this can be achieved via high-strength headed shear studs welded to the angle and affixed into the beam (or corbel) before concrete casting (see Fig. 5).

2.2.2. Moment connections

As presented in Table 1, two precast specimens with new type 2 moment connections were numerically studied. The first specimen P-MC-T2-ANG was the same as control specimen P–SC–T2-ANG, but with wet/dry beam-column connection having continuous top beam bars. Fig. 8 shows details of precast specimen P-MC-T2-ANG with the proposed type 2 moment connection. In this specimen, the top 90 mm thickness of both the original and reduced beam sections was made of CIS concrete for a distance of 1130 mm at both ends. The top beam bars were made continuous through the column using high strength couplers tied at the end of beam bars that were pre-constructed with the precast RC columns as seen in Fig. 8. Similar to specimen P-MC-T1-ANG, these couplers were utilized for mechanical splicing of the top beam bars in the wet connection region. These bars, in turn, were lap spliced with the pre-constructed top bars of the precast RC beam using class B tension splice [39]. The gap at the interface of the beam with the column was filled with non-shrink cementitious mortar (see Fig. 8). The second specimen with type 2 moment connection (P-MC-T2-PB_ANG) is the same as P-MC-T2-ANG but with full anchorage at the interface of angles with concrete of beam and corbel, as proposed in Fig. 5.

2.3. Monolithic specimens

As presented in Table 1, in addition to the 9 precast specimens, two assemblies that were designed with monolithic beam-column connections (M-CBR & M-DBR) were numerically investigated under the loss of the middle column. These assemblies were tested previously in Refs. [36,37], and they were used in the current study as control specimens for comparison with the precast assemblies. Details of monolithic specimens M-CBR and M-DBR, as taken from Refs. [36,37], are depicted in Fig. 9. It is clear from Fig. 9 that both specimens have the same dimensions and steel reinforcement as the precast specimens, except for the absence of the corbels. However, specimen M-CBR has continuous bottom and top beam bars in the connection zones to represent the case of intermediate RC moment frames used in the Western region of Saudi Arabia (as a moderate seismic zone). Even though specimen M-DBR was constructed with continuous top beam bars in the connection zones as seen in Fig. 9, the bottom beam bars were made discontinuous in the connection regions (see Fig. 9). This was done to represent the case of ordinary RC moment frames used in the non-seismic zones of Saudi Arabia (such as the city of Riyadh).

Table 2 presents the properties of materials used in studied specimens. The material properties in Table 2 were assumed the same as those used for constructing the tested control specimens P–SC–T1-NP, P–SC–T2-ANG, M-CBR, and M-DBR [36,37]. As mentioned previously, specimens were numerically investigated in this study under the loss of the middle column. This was done exactly similar to the loading protocol used in the testing of control specimens P–SC–T1-NP, P–SC–T2-ANG, M-CBR, and M-DBR [36,37]. In these experiments, a vertical loading was put on the middle column of the assembly in a displacement-controlled manner at a quasi-static rate of 100 mm/s to represent the progressive collapse event (see Fig. 10). Therefore, the inertial effects in tests were less than those anticipated in real progressive collapse incidents. Nevertheless, the increase in induced stresses owing to the inertial effects is partially substituted by the enhanced strength of materials owing to the effect of strain rate.

3. FE analysis

The 11 assemblies listed in Table 1 were modeled with the help of LS-DYNA software [40]. On account of the symmetry of the specimens, only one-half of the assembly was simulated.

3.1. Mesh generation

Figs. 11–13 show the FE mesh for precast specimens with types 1 and 2 connections, and monolithic specimens, respectively. Eight-node brick elements with reduced integration formula were utilized to represent the concrete volume of beams, corbels, and columns; cementitious grout; neoprene pads of precast specimen P–SC–T1-NP; and steel angles and plates used in the connections of other precast specimens. Two-node beam elements were utilized to simulate the reinforcing bars of all specimens. The I-beams of the base stubs were modeled using Belytschko-Tsay shell elements of four nodes [41], as presented in Figs. 11–13. In all FE models, the size of elements ranged from 2.5 to 100 mm. The sizing of elements was determined via mesh sensitivity analysis, and it was realized that more mesh refinement would have a minor impact on the numerical output; nevertheless, it may considerably extend the solution time.

3.2. Material modeling

The key input parameters of the material models utilized in the FE modeling are listed in Table 2. As the rate of load application was 100 mm/s, rate-dependent material models were used. Both concrete volume in all specimens and cementitious grout were modeled using the smooth surface cap material model (type 159). The general 2D shape of the yield surface is seen in Fig. 14. The viscoplastic rate effects are included. This constitutive model is further discussed and detailed in Refs. [40,42].

The piecewise linear plasticity model (type 24) was used to simulate steel reinforcement of all members, as well as angles and plates at connections of precast specimens. In this model, the strain-rate effect was incorporated by scaling the yield strength of steel bars using the following formula:

$$DIF_y = 1 + \left(\frac{\dot{\varepsilon}}{C}\right)^{1/p} \tag{1}$$

where DIF_y is the factor for scaling the yield stress; $\dot{\varepsilon}$ is the strain rate (in s^{-1}); and p and C are model parameters, inputted as 1.6 and 250, respectively [16]. The hyperelastic rubber model developed by Christensen [43] (type 77) was used to simulate the neoprene pads of precast assembly P–SC–T1-NP. For the I-shaped base stubs, the linear elastic constitutive model (type 1) was utilized.

Failure of concrete material and cementitious grout was simulated using strain-dependent erosion criteria. For element erosion, the threshold maximum principal tensile strain was input as 5% [42,44]. This aided in evading excessive element distortions. However, erosion of steel elements was represented by the threshold fracture plastic strain (reported in Table 2 for steel bars, plates, and angles).

3.3. Contact modeling

Figs. 11 and 12 show examples of modeled precast simple shear and moment connections. For all precast elements with simple shear connections, an automatic surface-to-surface contact was input between: (1) beams and inner/exterior columns; and (2) beams and inner/exterior corbels. However, for precast beams with moment connections, surface-to-surface contacts were defined between (1) cementitious grout and columns/beams; and (2) beams and inner/exterior corbels. It should be noted that in precast beams with moment connections, a full bond was assumed between the wet part of the beams and the columns. For control precast specimen P–SC–T1-NP, surface-to-surface contacts were assumed between neoprene pads and corbels/beams. Master and slave surfaces were input for each contact. A friction coefficient of 0.6 was input between contacted concrete surfaces [39], while a friction coefficient of 0.4 was input at the neoprene pad-to-concrete interface [45].

For precast specimens with angles/plate assembly at the connections

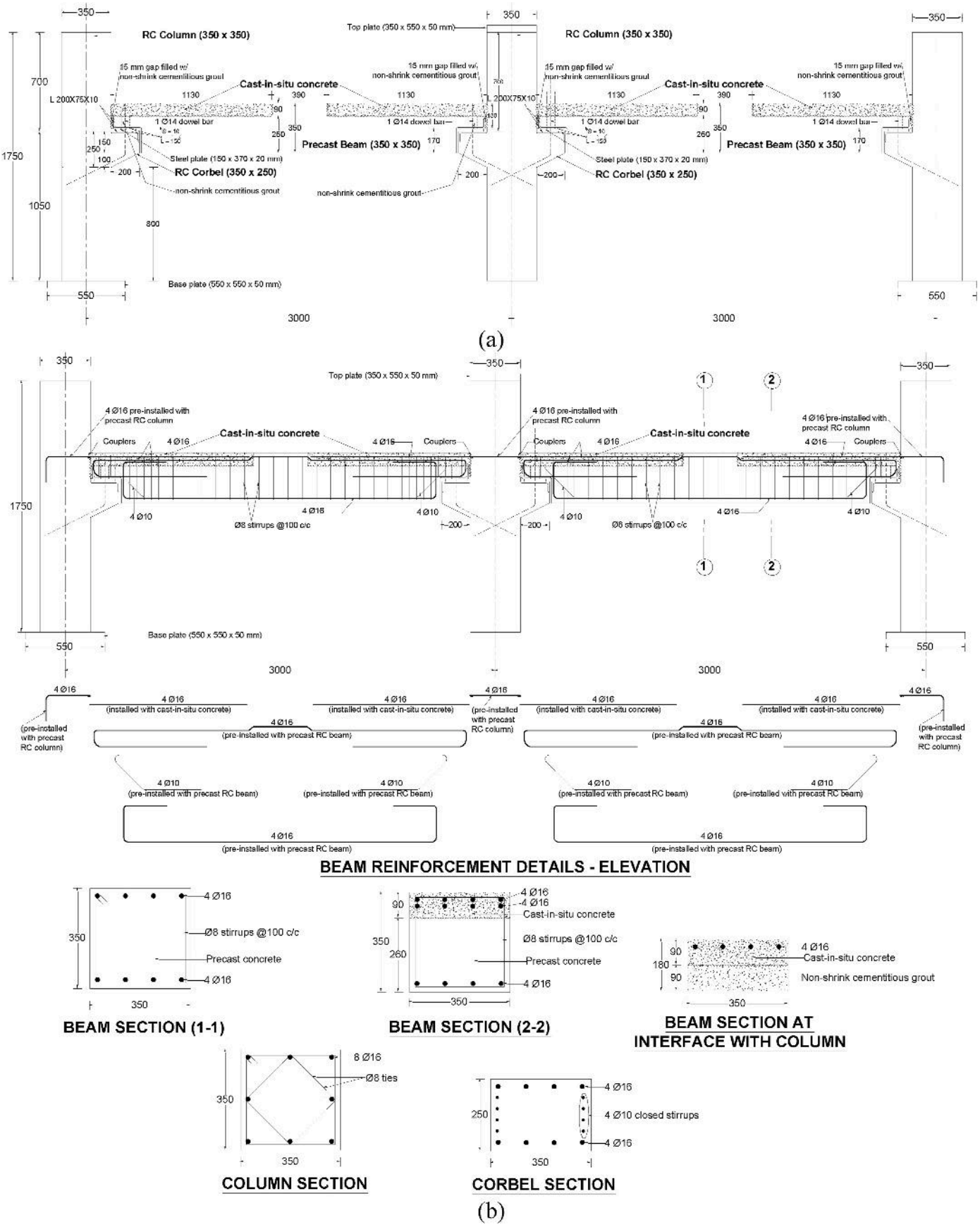

Fig. 8. Details of precast assembly P-MC-T2-ANG with type 2 moment connection (Dimensions are measured in mm): (a) Concrete dimensions; (b) Reinforcement.

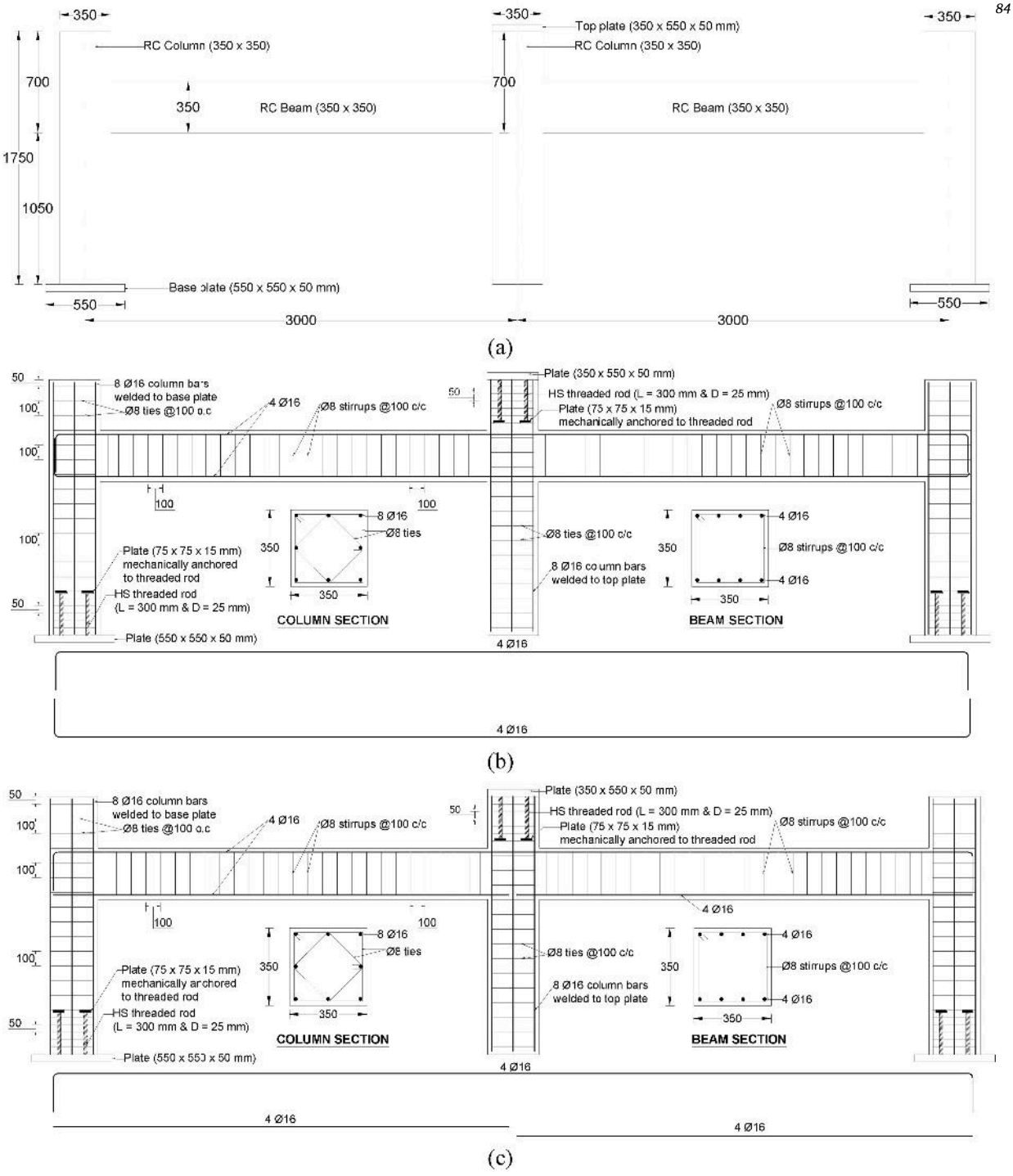

Fig. 9. Details of monolithic assemblies M-CBR and M-DBR [36,37] (Dimensions are measured in mm): (a) Concrete dimensions; (b) Reinforcement for M-CBR; (c) Reinforcement for M-DBR.

(P-SC-T1-ANG, P–SC–T1-PB_ANG, P-MC-T1-ANG, P-MC-T1-PB_ANG, P–SC–T2-ANG, P–SC–T2-PB_ANG, P-MC-T2-ANG, and P-MC-T2-PB_ANG), the generalized constrained fillet weld contact was employed to model welding at the angles-to-plate interface. However, for specimens P–SC–T1-ANG, P-MC-T1-ANG, P–SC–T2-ANG, and P-MC-T2-ANG, spot welding between steel angles and main reinforcement of beam and corbel was disregarded, and the interfacial shear stresses at angles-to-concrete interaction were mainly resisted by the interface adhesion. This was simulated with the help of the following formula of tiebreak surface-to-surface contact.

$$\left(\frac{|\sigma_n|}{\sigma_{n,F}}\right)^2 + \left(\frac{|\sigma_s|}{\sigma_{s,F}}\right)^2 \geq 1 \tag{2}$$

where σ_n & σ_s are, sequentially, the interfacial normal and shear stresses; and $\sigma_{n,F}$ & $\sigma_{s,F}$ are, in turn, the corresponding failure stresses, which were obtained from Ref. [38] as

$$\sigma_{n,F} = \sigma_{s,F} = 0.2\sqrt{f'_c} \qquad \text{(MPa)} \tag{3}$$

Table 2
Key input parameters for constitutive models of the FE analysis.

Concrete & cementitious grout				
Constitutive model	Type 159 (continuous surface cap model)			
Density (kg/m^3)	2320			
Uni-axial compressive strength (MPa)	35 and 60 for concrete and cementitious mortar, respectively			
Max aggregate size (mm)	10			
Steel bars, plates and angles	*ϕ8 mm*	*ϕ10 mm*	*ϕ16 mm*	*Plates and angles*
Constitutive model	Type 24 (piecewise linear plasticity model)			
Density (kg/m^3)	7850			
Elastic modulus (MPa)	200,000			
Poisson's ratio	0.3			
Strain-rate parameter, C	250			
Strain-rate parameter, *p*	1.6			
Yield strength (MPa)	525	489	526	240
Tangent modulus (MPa)	127	2127	1065	0
Plastic strain at fracture (%)	19.7	11.6	11.7	20
Neoprene pads				
Constitutive model	Type 77 (hyperelastic rubber model)			
Density (kg/m^3)	1100			
Poisson's ratio	0.499			
Shear modulus (MPa)	1.38			
Limit stress (MPa)	5.52×10^{-3}			
Constants C_{10}, C_{01}, C_{11}, C_{20}, C_{02}, C_{30}	0.55, 0, 0, −0.05, 0, 0.95			

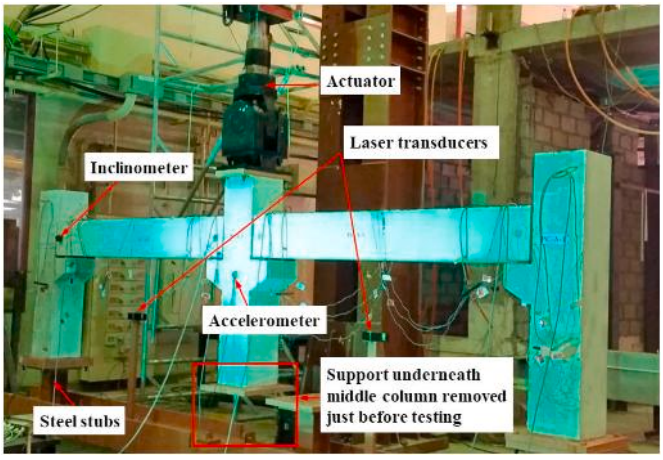

Fig. 10. Test setup for assembly P–SC–T1-NP [36,37].

where f_c' is the compressive strength of standard concrete cylinders. For precast specimens P–SC–T1-PB_ANG, P-MC-T1-PB_ANG, P–SC–T2-PB_ANG, and P-MC-T2-PB_ANG, a perfect bond was modeled at the interaction of angles with concrete of beam and corbel.

3.4. Bond-slip modeling

For all of the nine precast specimens investigated in the current study, a perfect bond was modeled at the interaction of reinforcing bars with concrete. This was assumed because as outlined in Refs. [36,37], slippage at the interface of beam bars with concrete was not observed during the testing of control precast specimens P–SC–T1-NP and P–SC–T2-ANG. For monolithic specimen M-CBR, a perfect bond was also modeled at the bars-to-concrete interface because bar slippage was not noted throughout the testing – as discussed in Refs. [36,37] – owing to the continuity of main beam bars in the joint zones. Nevertheless, for monolithic assembly M-DBR, a perfect bond was modeled at the interface of all bars with concrete except for the main bottom bars of the beams due to their discontinuity in the connection regions. For bottom bars in beams of specimen M-DBR, the bond-slip effect was modeled using the one-dimensional (1D) contact algorithm available in LS-DYNA [40]. Separate nodes were defined for both brick elements of concrete volume (master nodes) and beam elements of steel bars (slave nodes), and fictitious springs were assumed between the node couples as illustrated in Fig. 15(a). In the 1D contact model, accumulation of damage was not initially considered. The bond-slip relationship was taken as linear till the maximum bond shear stress value (τ_{max}), after which the damage accumulation was accounted for. Thereafter, the bond stress decreased with the increase of the plastic slip. The bond-slip relationship is then represented by the following equation.

$$\tau = \begin{cases} G_s s & s \le s_{max} \\ \tau_{max} e^{-h_{dmg} D} & s > s_{max} \end{cases} \quad (4)$$

where τ = bond shear stress; s = corresponding bar slip; G_s = shear modulus; s_{max} = peak elastic slip; h_{dmg} = parameter for the plastic portion of the curve; and D = damage coefficient.

In order to use the 1D contact model, the three parameters G_s, s_{max}, and h_{dmg} are needed as input. Since the beam-column connection regions in specimen M-DBR represent the case of ordinary moment RC frames, in which concrete may be considered unconfined by transverse ties, the bond-slip model developed by Xiao and Rui [46] for unconfined concrete was employed for calibrating the input parameters of the 1D contact model. A value of 0.254 mm was input for the peak elastic slip s_{max}. The bond shear strength value (τ_{max}) was estimated from the following equation proposed by ACI 408R-03 [47].

$$\tau_{max} = 20 \frac{\sqrt{f_c'}}{d_b} \le 5.52 \ \text{MPa} \quad (5)$$

where f_c' is the compressive strength of standard concrete cylinders (in MPa units), and d_b is the diameter of the steel bar (in mm). Therefore, the bond shear modulus G_s was input in the model as

$$G_s = 78.74 \frac{\sqrt{f_c'}}{d_b} \le 21.73 \ \text{MPa} \quad (6)$$

For the exponential parameter h_{dmg}, three values were calibrated with the bond-slip model of Xiao and Rui [46] as illustrated in Fig. 15(b). The first value of 0.05 was taken as per the study of Elsanadedy et al. [48] on the robustness of RC special moment frames to progressive collapse. The second value of 0.24 was assumed based on the pullout test data of Tepfers and Olsson [49]. The input bond-slip curves of the first two values (0.05 and 0.24) are plotted in Fig. 15(b), and they are then compared with that of Xiao and Rui [46]. As seen from the figure, these two curves significantly overestimate the post-peak bond shear stress in the plastic zone. Thus, the third value of h_{dmg} = 0.90 was suggested in this study to have a good agreement with the curve of Xiao and Rui [46], as presented in Fig. 15(b).

3.5. Boundary conditions and loading protocol

On account of the symmetry of the investigated assemblies, one-half of the frame assembly was numerically modeled. As seen in Figs. 11–13, the supports underneath the steel stubs of the exterior columns were fixed by preventing the displacement in the global Cartesian coordinate system (X, Y, and Z) for the bottom nodes of the brick elements of the base steel plate. Boundary conditions representing symmetry were input for the nodes on the YZ plane passing through the middle column as shown in Figs. 11–13. A linear downward (in the negative Z-direction) displacement-time history of 100 mm/s was applied on the top nodes of the middle column (see Fig. 16). This was done to represent the quasi-static loading protocol utilized in the testing of control assemblies P–SC–T1-NP, P–SC–T2-ANG, M-CBR, and M-DBR [36,37].

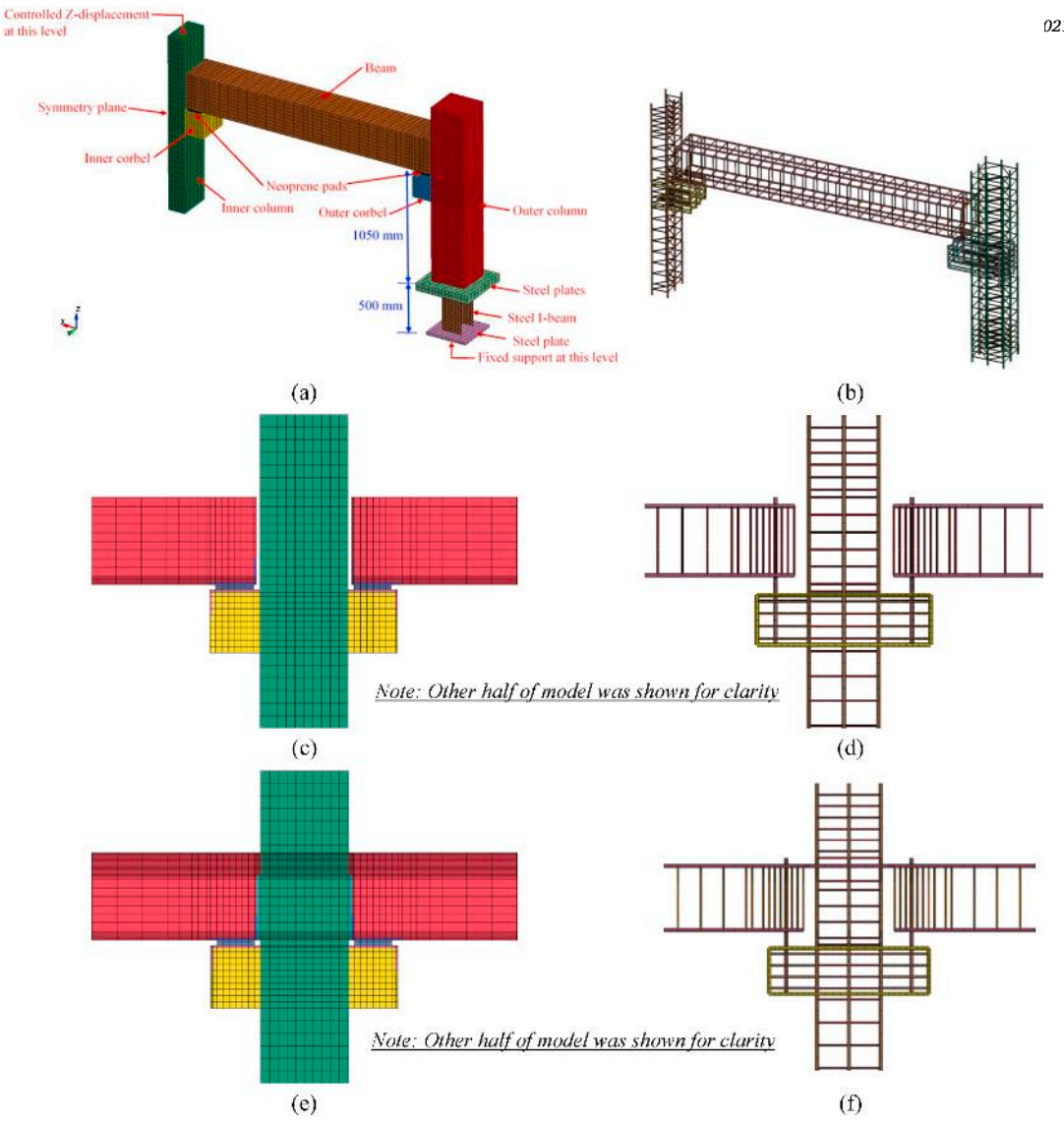

Fig. 11. FE model for precast assemblies with type 1 connections: (a) One-half of P–SC–T1-NP; (b) Reinforcement for one-half of P–SC–T1-NP; (c) Middle connection of P–SC–T1-ANG and P–SC–T1-PB_ANG; (d) Reinforcement of middle connection of P–SC–T1-ANG and P–SC–T1-PB_ANG; (e) Middle connection of P-MC-T1-ANG and P-MC-T1-PB_ANG; (f) Reinforcement of middle connection of P-MC-T1-ANG and P-MC-T1-PB_ANG.

4. Model calibration

It should be noted that the numerical models of four specimens (out of the 11 studied beam-column assemblies) were validated. The FE models of control specimens P–SC–T1-NP, P–SC–T2-ANG, and M-CBR were validated in a previous study by Elsanadedy et al. [38] using the test results available in Ref. [36]. However, in the current study the test results of specimen M-DBR, detailed in Ref. [37], were used to validate the bond-slip modeling discussed in Sec. 3.4.

As outlined previously, bond-slip modeling was considered for the bottom bars in beams of monolithic specimen M-DBR. In this regard, four different numerical models were created. The first model (Case 1) is supposed to give an upper bound solution, and it is for the analysis with perfect bond at the interface of main reinforcement with concrete. The second model (Case 2) is for the analysis with bond-slip effects considering $h_{dmg} = 0.05$, as proposed by Elsanadedy et al. [48] for special moment RC frames. In the third model (Case 3), the FE analysis considered bond-slip effects with $h_{dmg} = 0.24$, as per the pullout test results of Tepfers and Olsson [49]. However, the last model (Case 4) incorporated bond-slip modeling with $h_{dmg} = 0.90$, as proposed in this study based on calibrating the bond-slip curve of the 1D contact model with that of Xiao and Rui [46] (refer to Sec. 3.4). Fig. 17(a) presents the comparison between the load versus displacement curves outputted from the four analysis models and the experiment (as obtained from Ref. [37]). It is noted that the assumption of perfect bond in Case 1 significantly overestimated the load-displacement response in terms of stiffness and peak load, with an experimental-to-numerical peak load ratio of 0.68. The analysis in cases 2 and 3 also overestimated the response with experimental-to-numerical peak load ratios of 0.86 and 0.94, respectively. Nevertheless, as presented in Fig. 17(b), the FE model of Case 4 (with $h_{dmg} = 0.90$) agreed well with the experiment with an experimental-to-numerical maximum load ratio of 1.01. Fig. 17(b) depicts the experimentally observed failure mode at the middle connection of specimen M-DBR at the end of the test (as taken from Ref. [37]). As seen from the figure, full slippage of the bottom bars of the beam was noticed towards the end of the test, as identified by the large flexural cracks in the beam-column interface. The FE mode of failure of Case 4 (with $h_{dmg} = 0.90$) is illustrated in Fig. 17(c) for the middle connection of assembly M-DBR at the end of the analysis. Displayed in Fig. 17(c) are the damage contours varying from 0 to 1, where 0 indicates no damage

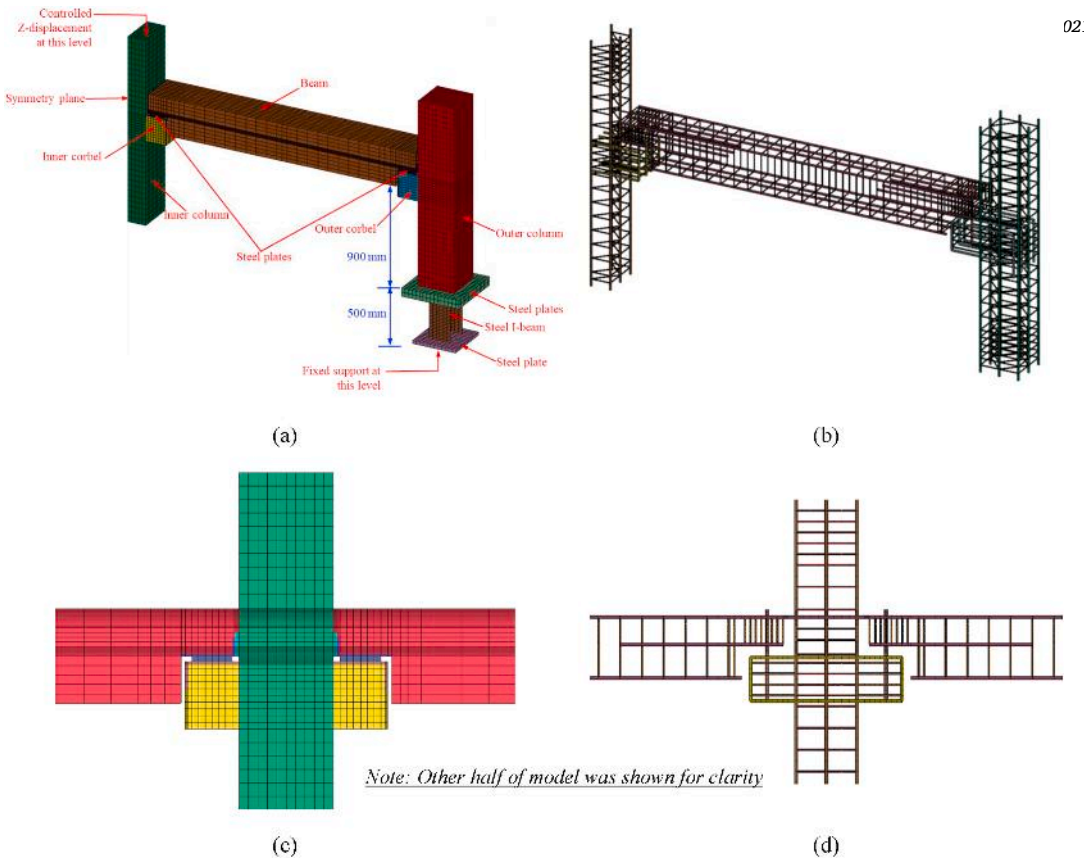

Fig. 12. FE model for precast assemblies with type 2 connections: (a) One-half of P–SC–T2-ANG; (b) Reinforcement for one-half of P–SC–T2-ANG; (c) Middle connection of P-MC-T2-ANG and P-MC-T2-PB_ANG; (d) Reinforcement of middle connection of P-MC-T2-ANG and P-MC-T2-PB_ANG.

and 1 indicates full damage. The predicted failure mode agreed well with the experimental results. Slippage of tension steel bars of the beam was predicted at the middle connection. This was indicated by the wide flexural cracks in the beam section close to the middle column, as seen in Fig. 17(c).

5. Discussion of FE results

The key analysis results for all assemblies are presented in Table 3. The ultimate state outlined in Table 3 is considered as corresponds to a 20% drop in the peak load [50]. The energy dissipated, listed in Table 3, is calculated as the area under the curve of load versus middle column displacement up to the onset of concrete crushing in the beam at the inner column face. In the subsequent subsections, the FE results are discussed with regard to failure modes, load versus displacement characteristics, and analysis of strain gage results.

5.1. Failure modes

Figs. 18–21 display the FE failure modes for investigated specimens in terms of damage (effective plastic strain) contours for the middle and exterior connections. These contours vary from 0 to 1, where 0 indicates no damage and 1 indicates full damage. Follows is a discussion of the numerically predicted failure modes for various groups.

5.1.1. Precast specimens with type 1 simple connections

Fig. 18(a)–(c) display damage contours for precast assemblies with type 1 simple connections. It is clear that for control specimen P–SC–T1-NP, a typical hinge behavior was predicted. Under increased middle column displacement, both precast beams rotated until the top beam ends touched the center column. As illustrated in Fig. 18(a), the ultimate mode of failure was owing to crushing of concrete at the beam end. Nevertheless, for the outer connection, no damage was observed as shown in Fig. 18(a).

For specimen P–SC–T1-ANG in which the neoprene pads were replaced with angles/plate assembly, failure at the middle connection commenced with debonding at corbel/angle interface, and it was ultimately owing to crushing of concrete at the end of precast beams, as noted in Fig. 18(b). Failure was a little different at the exterior connection as shown in Fig. 18(b). It was initially owing to debonding at the interface of corbel with steel angle and ended up with partial damage of the corbel concrete.

When the perfect bond was assumed at the interface of angles with concrete in specimen P–SC–T1-PB_ANG, debonding at corbel/angle interface was mitigated at both middle and exterior connections, as noted in Fig. 18(c). However, in the middle connection, concrete at the interface of steel angles with beam and corbel was damaged at large levels of center column displacement, and the failure was ultimately owing to concrete crushing at the end of beams together with partial damage of concrete cover of the middle column above the middle corbel, as noted in Fig. 18(c).

5.1.2. Precast specimens with type 1 moment connections

Failure modes of precast assemblies with type 1 moment connections are shown in Fig. 19(a) and (b). For specimen P-MC-T1-ANG, failure of the middle connection started at early middle column displacement owing to debonding at corbel/angle interface. With increased displacement, damage occurred at steel angle/beam interface, and flexural cracking of infill grout was predicted in the gap at the beam-column interface. This cracking went all the way up to the level of top continuous beam bars in the added wet concrete layer as seen in Fig. 19(a). Ultimate failure was owing to crushing of the top added concrete

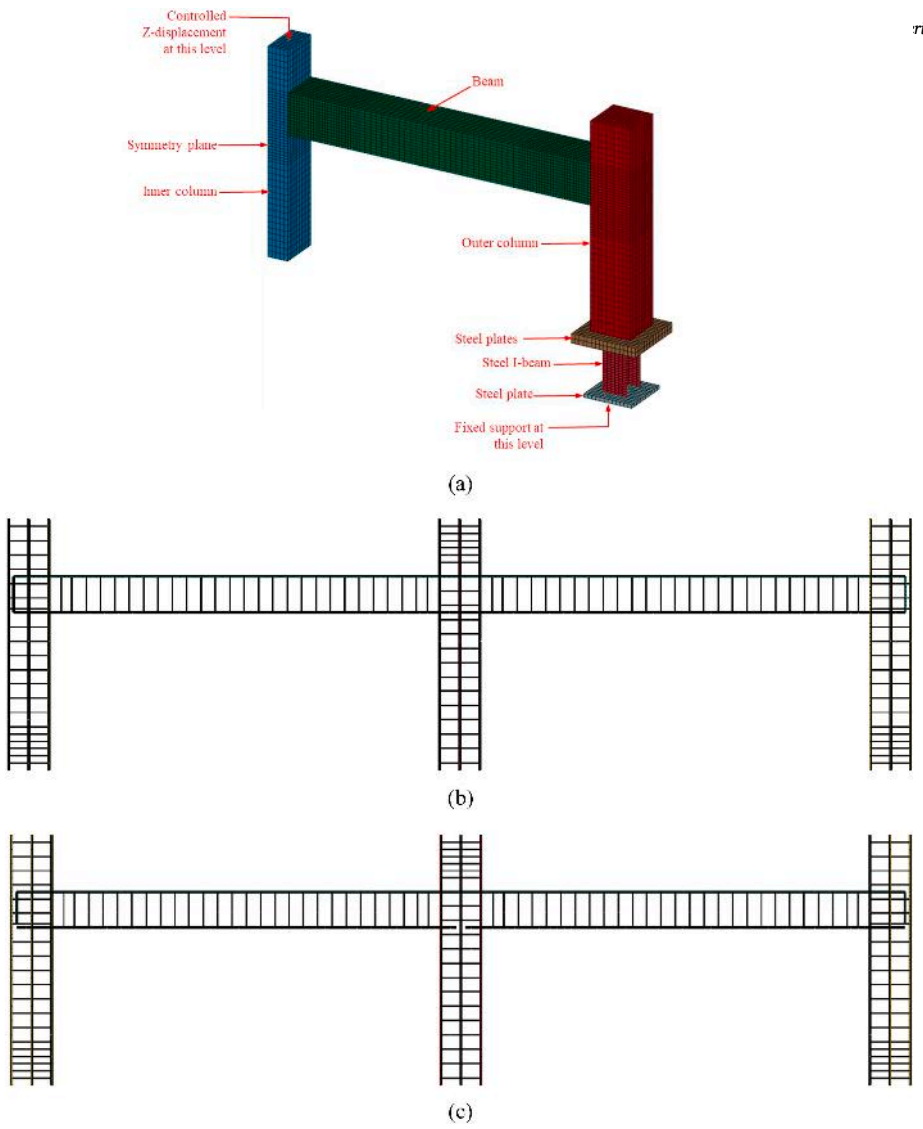

Fig. 13. FE model for monolithic assemblies M-CBR and M-DBR: (a) One-half of assembly; (b) Reinforcement of M-CBR; (c) Reinforcement of M-DBR.

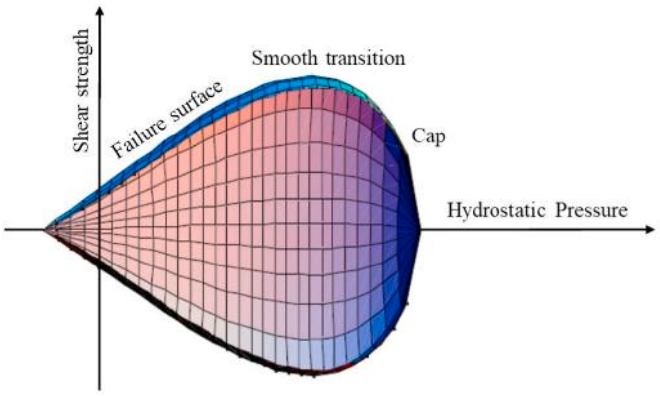

Fig. 14. General 2D shape of yield surface of the concrete model type 159 [40].

layer close to the face of the middle column (see Fig. 19(a)). In this connection, the plastic hinge was localized in the wet added concrete layer near the column face. Nevertheless, in the exterior connection, a full plastic hinge was formed at the beam section near the face of the exterior corbel. This plastic hinge was identified by large flexural cracking associated with crushing of concrete at large displacement levels as seen in Fig. 19(a).

When the perfect bond was assumed at the interface of steel angles with concrete in specimen P-MC-T1-PB_ANG, debonding at corbel/angle interface was inhibited at middle connections, as noted in Fig. 19(b). Nevertheless, at early displacement of the center column, concrete was damaged at the corbel/angle interface. At large displacement levels, this damage extended into both the corbel and the concrete cover of the middle column directly above the inner corbel, as noted in Fig. 19(b). Furthermore, damage occurred in the concrete at the interface of the beam with steel angle, and flexural cracking of infill grout was predicted in the gap at the beam-column interface. Similar to specimen P-MC-T1-ANG, this flexural cracking propagated up to the level of top continuous beam bars in the added wet concrete layer, and the final failure of the middle connection was owing to crushing of the top concrete layer at column interface (see Fig. 19(b)). It was also clear that the plastic hinge in the middle connection was localized in the top added concrete layer close to the column face. Nevertheless, in the exterior connection, a plastic hinge was fully developed at the beam section close to the face of the exterior corbel. This was identified by large flexural cracking and crushing of concrete as shown in Fig. 19(b).

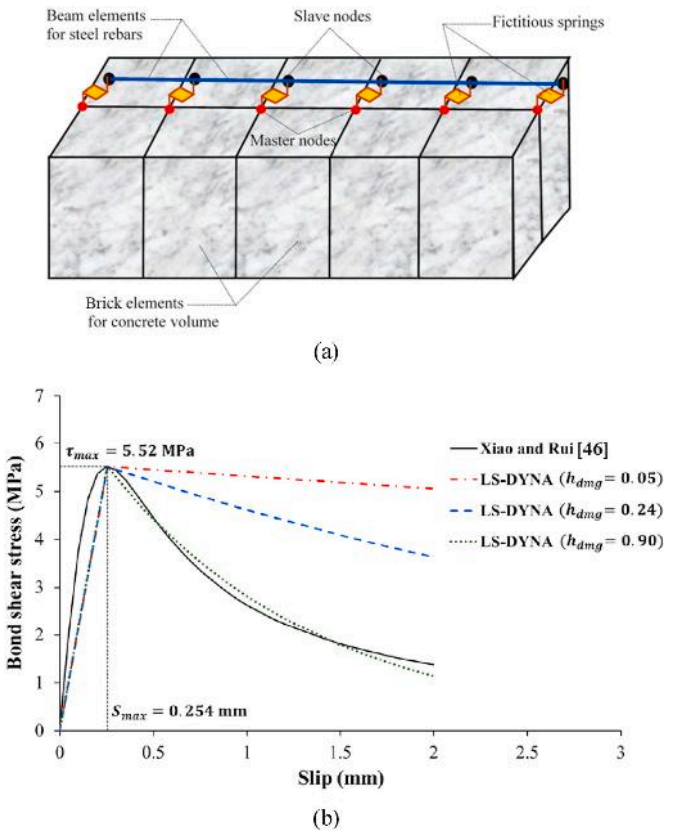

Fig. 15. 1D contact model used in monolithic assembly M-DBR: (a) Fictitious springs between brick and beam elements; (b) Calibration of bond-slip model.

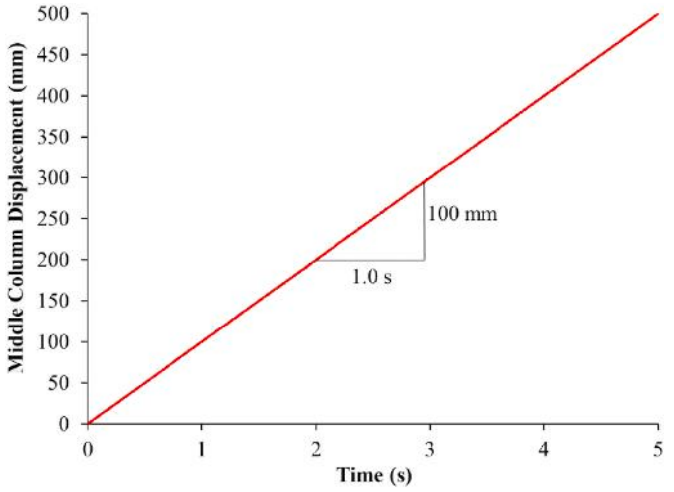

Fig. 16. Displacement-time history applied on the top nodes of the middle column.

5.1.3. *Precast specimens with type 2 simple connections*

Fig. 20(a) and (b) present modes of failure for precast specimens with type 2 simple connections. For specimen P–SC–T2-ANG, a typical hinge behavior was predicted in both middle and exterior connections. The precast beams rotated at the ends until failure, which was owing to debonding at corbel/angle interface as noted in Fig. 20(a) for interior and exterior connections.

The assumption of the perfect bond at the interface of steel angles with concrete affected the mode of failure of specimen P–SC–T2-PB_ANG, and debonding was mitigated. However, at large displacement levels, concrete at angles/corbel (beam) interface got damaged, and the ultimate failure of the interior connection was owing to crushing of concrete at the beam end. This failure was accompanied by damage of the concrete cover of the middle column directly above the middle corbel, as displayed in Fig. 20(b). Nevertheless, for outer connections, the ultimate failure was owing to damage of concrete at angle/corbel interface, extending into column concrete. This was combined with concrete damage at end of the beam, as presented in Fig. 20(b).

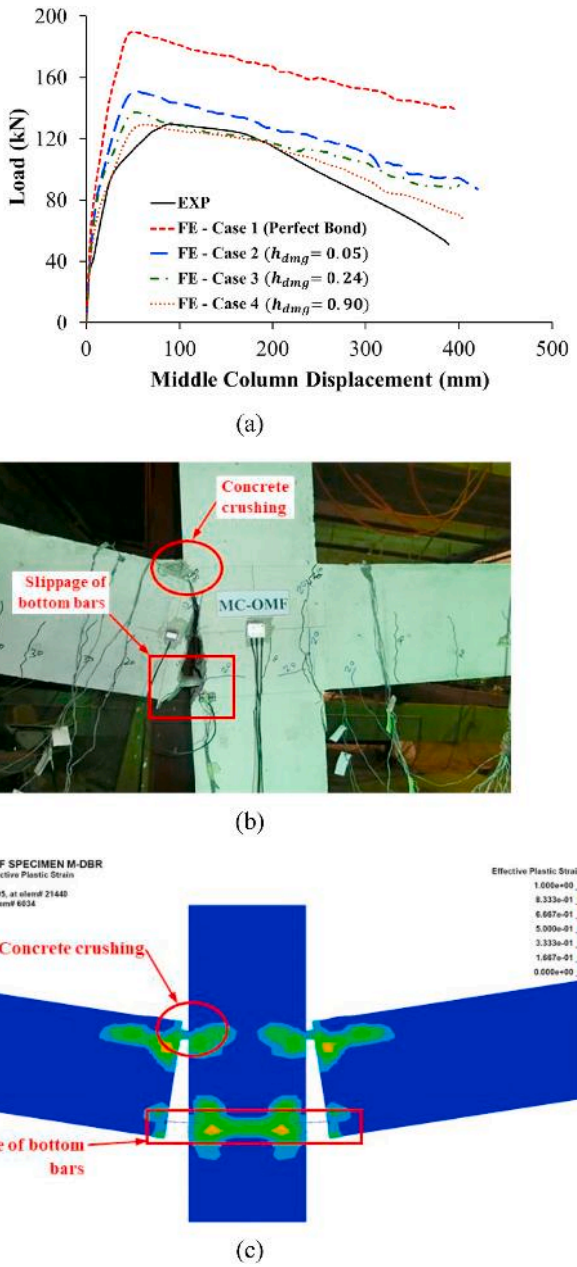

Fig. 17. Calibration of FE modeling for monolithic assembly M-DBR: (a) Experimental versus FE load-displacement curves; (b) Experimental failure mode at middle connection [37]; (c) FE failure mode at middle connection.

5.1.4. *Precast specimens with type 2 moment connections*

Fig. 21(a) and (b) display damage contours for precast assemblies with type 2 moment connections. As noted in Fig. 21(a), the failure of specimen P-MC-T2-ANG was almost similar to specimen P-MC-T1-ANG. Failure of the middle connection started at early displacement levels due to debonding at corbel/angle interface (see Fig. 21(a)). With increased displacement levels, flexural cracking occurred for the infill grout in the

Table 3
Key numerical results for studied assemblies*.

Assembly ID	Max. load (kN)	Displacement of middle column at max. load (mm)	Displacement of middle column at ultimate state (mm)	Dissipated energy (kN. m)	Peak strain in steel reinforcement (με)					
					Beam bottom bars at inner joint**	Beam top bars at inner joint	Beam top bars at outer joint***	Outer bars of exterior column	Top bars of interior corbel	Dowel bars of interior corbel
Precast specimens with type 1 connections										
P–SC–T1-NP	13	160	243	2.5	58	−106	41	62	330	***36616***
P–SC–T1-ANG	31	210	231	6.0	413	−110	82	411	421	***238092***
P–SC–T1-PB_ANG	108	170	194	14.5	***2674***	−487	200	692	***3569***	***150554***
P-MC-T1-ANG	162	65	246	35.1	294	***15057***	***87911***	2604	1607	***152918***
P-MC-T1-PB_ANG	224	40	55	39.0	2399	***11956***	***103280***	***3712***	***4373***	***144611***
Precast specimens with type 2 connections										
P–SC–T2-ANG	24	260	285	5.0	105 (690)	−127	456	166	759	***151078***
P–SC–T2-PB_ANG	52	245	270	10.7	635 (2065)	−132	1592	1057	1025	***106988***
P-MC-T2-ANG	107	245	265	19.7	370 (1030)	***21490***	***76479***	2402	1469	***116018***
P-MC-T2-PB_ANG	110	145	261	25.0	732 (***18977***)	***23672***	***76425***	2481	***3985***	***128411***
Monolithic specimens										
M-CBR	218	145	335	67.4	***102065***	***7739***	***13183***	***17236***	–	–
M-DBR	129	75	290	34.3	2496	***3703***	***25210***	***19469***	–	–

* Strains in bold italic font are higher than their corresponding steel yield strains.
** Values between brackets are strains in bars at mid-depth of beam at middle corbel face.
*** Strains in top beam bars at face of outer corbel and outer column for precast and monolithic specimens, respectively.

gap at the beam-column interface. This cracking propagated up to the level of top continuous beam bars in the added concrete layer as displayed in Fig. 21(a). The ultimate failure of the middle connection was due to crushing of the top concrete layer at the column interface. The plastic hinge was localized in the added concrete layer close to the face of the middle column. Nevertheless, in the exterior connection, a plastic hinge was fully developed in the reduced beam section adjacent to the face of the exterior corbel. This was identified by large flexural cracking associated with concrete crushing as noted in Fig. 21(a).

It is also noted from Fig. 21(b) that the failure of specimen P-MC-T2-PB_ANG was almost identical to that of specimen P-MC-T1-PB_ANG. Assuming perfect bond at the interface of steel angles with concrete in specimen P-MC-T2-PB_ANG mitigated debonding at the middle connection. At small displacement levels, concrete was damaged at corbel/angle interface, and at large displacement levels, this damage extended into both the corbel and the column concrete cover at corbel/column interface as seen in Fig. 21(b). Additionally, concrete in precast beams got damaged at their interface with angles. Flexural cracking also occurred for the infill grout in the gap at the beam-column interface and propagated up to the level of top continuous beam bars in the added concrete layer. The ultimate failure of the interior connection was owing to crushing of the top concrete layer at the column interface (see Fig. 21(b)), and the plastic hinge was localized in the beam adjacent to the interior column. Nevertheless, in the exterior connection, the plastic hinge was fully developed in the reduced beam section adjacent to the face of the exterior corbel (Fig. 21(b)).

5.1.5. Monolithic specimens

Fig. 22(a) and (b) present the FE failure mode for the CIS concrete assembly having continuity in the top and bottom beam reinforcement (assembly M-CBR). At large levels of center column displacement, a plastic hinge was developed in the beam adjacent to the interior joint region as identified by the large flexural cracking associated with concrete crushing in the top edge, as seen in Fig. 22(a). At the exterior connection, a plastic hinge was created in the beam region adjacent to the joint, along with cracking of the exterior column close to the connection region (see Fig. 22(b)). For the monolithic specimen with discontinuous beam bars (specimen M-DBR), the numerically predicted failure mode has been discussed previously in Sec. 4.

5.2. Load-displacement characteristics

Fig. 23(a) and (b) present comparisons between the numerically predicted load versus center column displacement curves for precast specimens with types (1) and (2) connections, respectively. The load-displacement curves for monolithic specimens M-CBR and M-DBR are also presented in Fig. 23. It is generally identified that the progressive collapse capacities in the flexural action stage of precast specimens with type (1) connections are noticeably higher than those for their type (2) counterparts. This is owing to the reduction in the beam section for type (2) connections at the corbel interface.

5.2.1. Precast specimens with type (1) connections

As clarified from Fig. 23(a), the control precast specimen P–SC–T1-NP with neoprene pad had a very poor load-displacement response with a very low peak load of 13 kN, as shown in Table 3. Replacing the neoprene pads in specimen P–SC–T1-NP with steel angles/plate assembly in specimen P–SC–T1-ANG enhanced the load-displacement response. The progressive collapse capacity (maximum load) and dissipated energy increased by 138% and 140%, in turn, as noted in Fig. 23(a) and Table 3 for assembly P–SC–T1-ANG. When the perfect bond was assumed at the interface of concrete with steel angles for assembly P–SC–T1-PB_ANG, both maximum load and dissipated energy increased by 248% and 142%, in turn, compared with assembly P–SC–T1-ANG.

Fig. 23(a) depicts that the new type (1) moment connections have improved load-displacement response compared with the type (1)

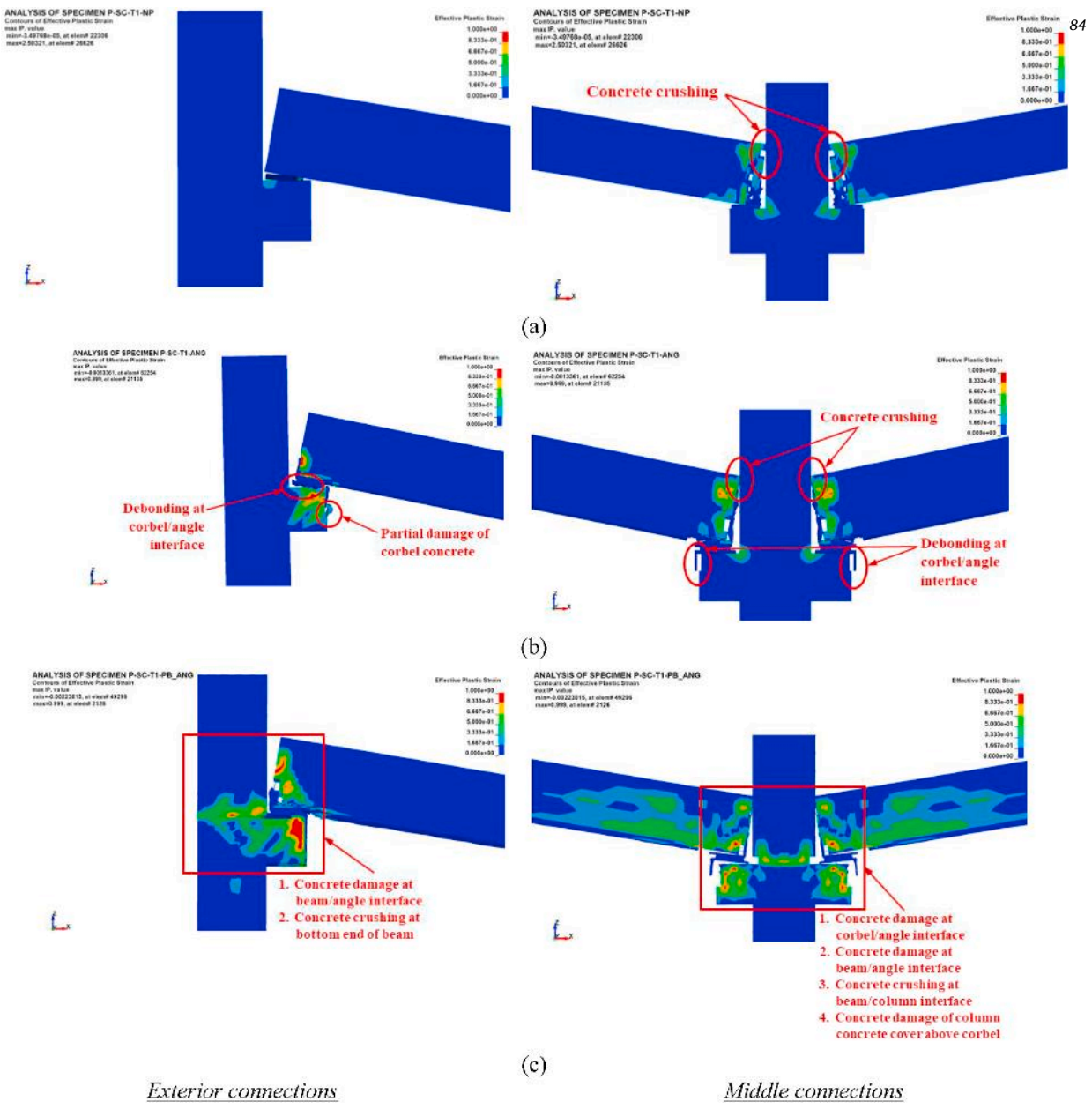

Fig. 18. Damage contours for: (a) P–SC–T1-NP; (b) P–SC–T1-ANG; (c) P–SC–T1-PB_ANG.

simple shear connections. Even when compared with monolithic specimen M-DBR having discontinuous bottom beam bars (representing the case of ordinary moment RC frames), the type (1) moment connection specimens P-MC-T1-ANG and P-MC-T1-PB_ANG had better load-displacement characteristics as seen from Fig. 23(a). However, their peak load and dissipated energy were less than the monolithic specimen M-CBR with continuous bottom and top beam bars. It should be noted that the flexural resistance of type (1) moment connections was due to a combination of two components at the middle connection zone: the partial contribution of the discontinuous bottom beam bars and the full contribution of the top continuous beam bars. In the middle connection, tensile stresses in the discontinuous bottom beam bars were transferred to the steel angles/plate assembly that in turn transferred them to the top corbel bars. As seen in Fig. 23(a), this was ideal for specimen P-MC-T1-PB_ANG until middle column displacement of 40 mm at which damage was initiated at angle/corbel interface, which resulted in a sudden drop in the load. With increased displacement, damage level at angles/concrete interface increased, and hence the contribution of the top corbel bars in the flexural resistance decreased. At this stage, the flexural capacity of the beam section at the middle column face was mainly generated from the contribution of the top continuous beam bars. At a displacement of 265 mm, the top concrete layer crushed in compression at the column face leading to a sudden drop in the load resistance as noted in Fig. 23(a). Nevertheless, for specimen P-MC-T1-ANG, debonding at angle/corbel interface occurred in the middle connection at early displacement levels. This has led to the partial contribution of bottom bars in the flexural strength of the assembly. The flexural capacity of the beam section at the middle column face relied mainly on the contribution of the top beam bars. As seen in Fig. 23(a), the load dropped suddenly for specimen P-MC-T1-ANG at a displacement of 245 mm owing to concrete crushing in the top layer at the middle column interface.

5.2.2. Precast specimens with type (2) connections

As shown from Fig. 23(b) and Table 3, the control precast specimen P–SC–T2-ANG with angles/plate assembly had a poor load-displacement

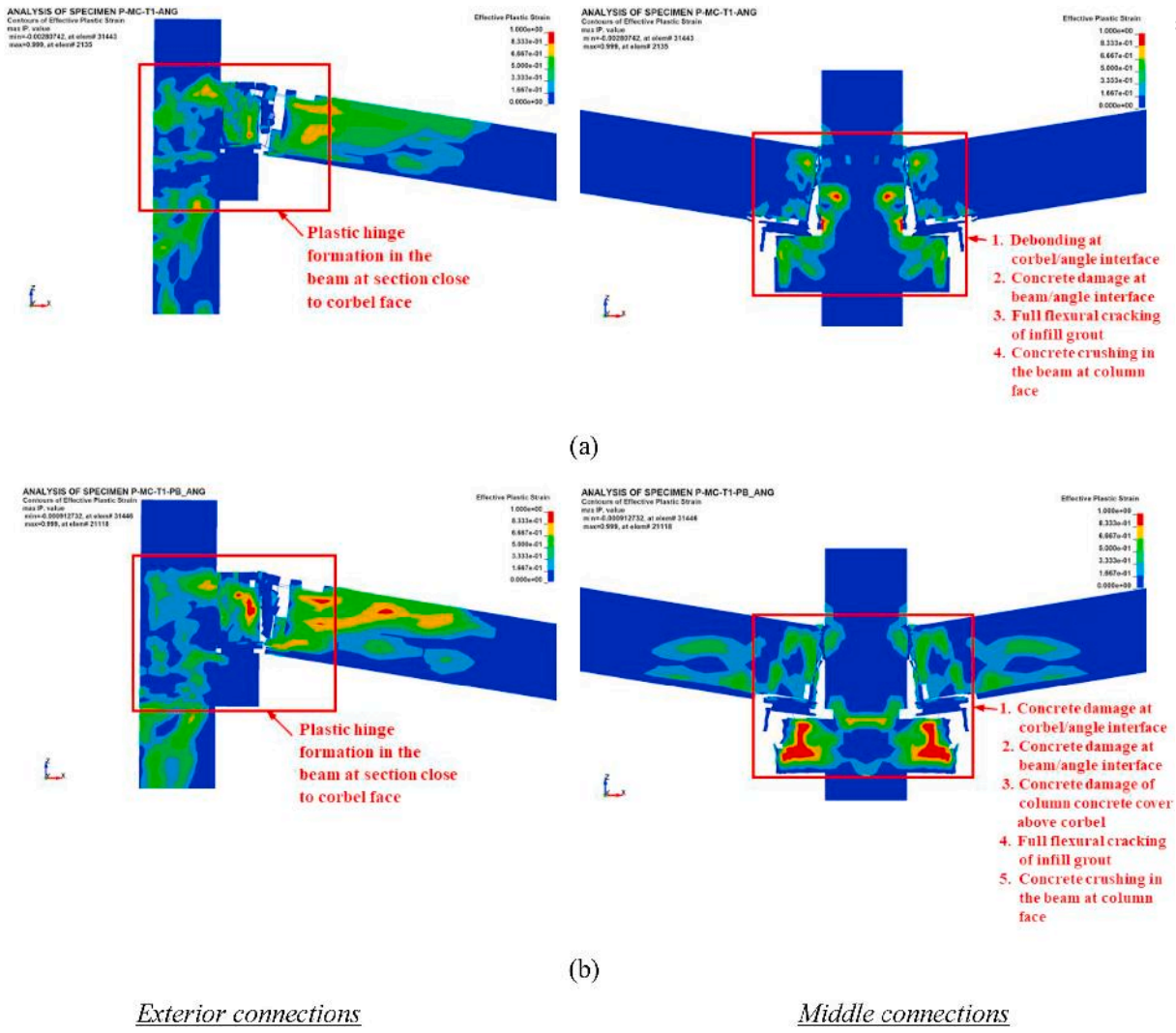

Fig. 19. Damage contours for: (a) P-MC-T1-ANG; (b) P-MC-T1-PB_ANG.

response with a very low peak load of 24 kN. When the perfect bond was assumed at the interface of steel angles with concrete for assembly P–SC–T2-PB_ANG, both maximum load and dissipated energy increased by 117% and 114%, respectively, compared with assembly P–SC–T2-ANG.

It is clear from Fig. 23(b) that the new type (2) moment connections have improved load-displacement characteristics compared with their simple shear connections. Owing to the assumption of the perfect bond at the interface of angles with concrete, the load-displacement response of specimen P-MC-T2-PB_ANG was better than specimen P-MC-T2-ANG in terms of maximum load and dissipated energy (see Table 3 and Fig. 23 (b)). However, owing to the reduction in the beam section at the critical section of the middle connection, their peak load and dissipated energy were less than both monolithic specimens M-CBR and M-DBR. Similar to type (1) moment connections, the flexural resistance of type (2) moment connections was due to a combination of two components at the middle connection zone: the partial contribution of the discontinuous bars at mid-depth of the beam at the inner corbel face and the full contribution of the top continuous beam bars. Tensile stresses in the discontinuous bars at mid-depth of the beam at the inner corbel face were transferred to the steel angles/plate assembly that in turn transferred them to the top corbel bars. At early displacement levels, debonding and concrete damage at angle/corbel interface, respectively, have occurred for specimens P-MC-T2-ANG and P-MC-T2-PB_ANG. This resulted in a partial contribution of bars at mid-depth of the beam in the flexural strength of the assembly. At the middle column face, the flexural capacity of the beam section relied mainly on the contribution of the top beam bars. As noted in Fig. 23(b), the load resistance of the two specimens increased at a displacement of 195 mm owing to the bearing of the bottom end of precast beams against the exterior corbels (see Fig. 21), which resulted in reduced beam rotation at the exterior connections and hence increasing the load capacity. However, at a displacement of 250 mm, the flexural resistance of the two specimens dropped suddenly owing to concrete crushing at the middle column interface as seen in Fig. 23(b).

It is evident from the load-displacement response shown in Fig. 23 that the behavior of all investigated specimens is mainly controlled by the flexural action, and the catenary action phase was not developed in any of the assemblies. This is owing to the inadequate restraint given by exterior columns and the discontinuity of beams past the outer columns. Even though catenary-action type bumps were observed in the load-displacement curve of few specimens such as P–SC–T1-PB_ANG, P–SC–T2-PB_ANG, P-MC-T2-ANG, and P-MC-T2-PB_ANG, this is not considered as the partial or full development of the catenary action stage. As clarified from previous studies on progressive collapse potential of RC moment frames, catenary action is initiated when the displacement at the removed column location exceeds the beam depth [26,48]. However, the bumps seen in Fig. 23 are initiated at middle column displacements that are significantly less than the beam depth (100 mm for specimen P–SC–T1-PB_ANG and 200 mm for assemblies

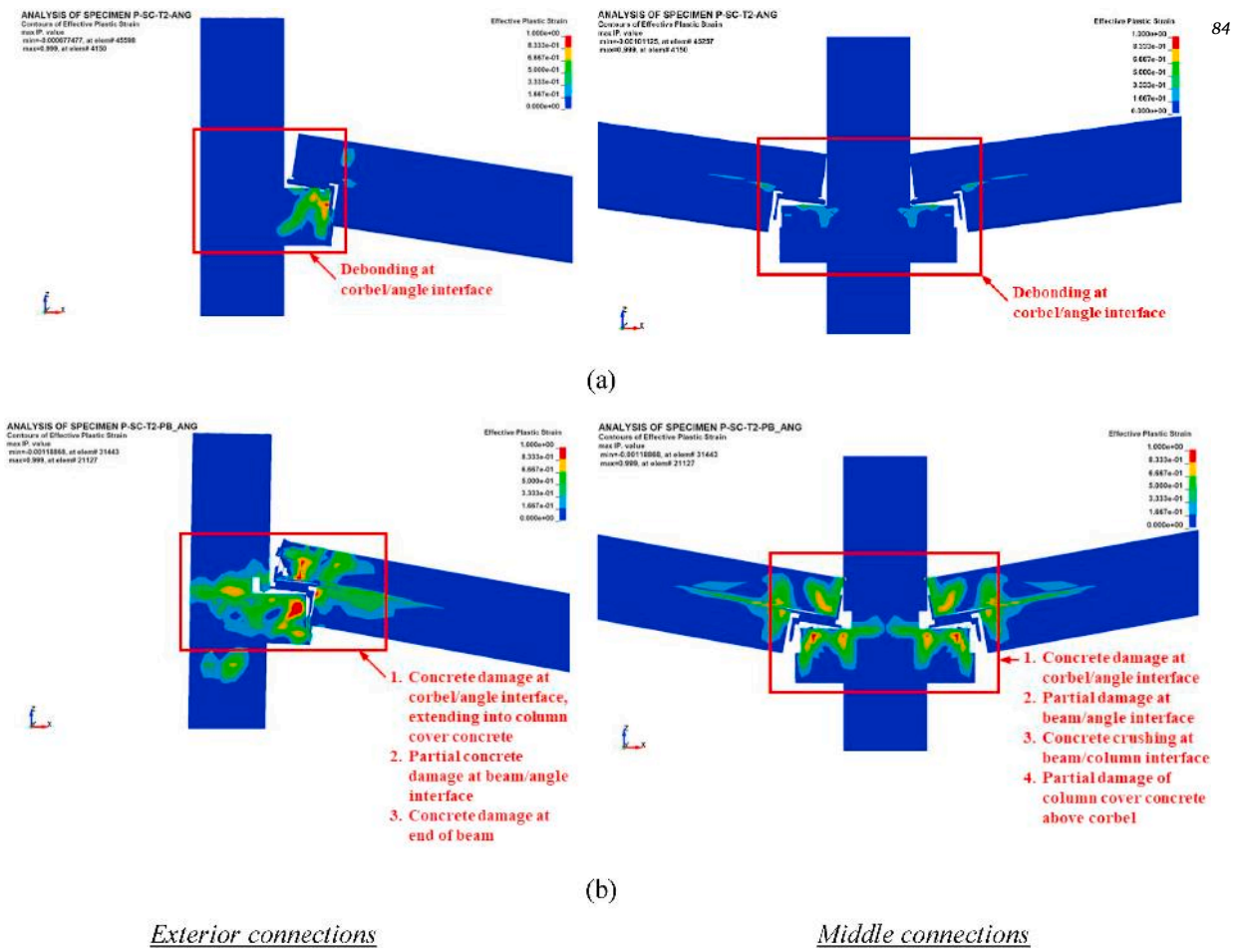

Fig. 20. Damage contours for: (a) P–SC–T2-ANG; (b) P–SC–T2-PB_ANG.

P–SC–T2-PB_ANG, P-MC-T2-ANG, and P-MC-T2-PB_ANG).

5.3. Strain gage results

Figs. 24–26 illustrate plots of the numerically predicted strain in steel bars at different locations versus displacement of middle column for precast and monolithic specimens. Table 3 also lists peak strain values in steel bars at different locations for all studied specimens. Follows are discussions of strain gage results of different groups.

5.3.1. Precast specimens with type 1 connections

Fig. 24(a) and (b) show, respectively, strains in the bottom reinforcement of the beam at the face of the interior corbel and the top reinforcement of the interior corbel at the face of the middle column. As noted from the figures and Table 3, very low tensile strains were recorded for control specimen P–SC–T1-NP with neoprene pads. For specimens with regularly attached steel angles (P-SC-T1-ANG and P-MC-T1-ANG), tensile strains in bottom beam bars and top corbel bars at the middle connection increased, but due to debonding at angle/corbel interface, they were still lower than the yield strain. When the perfect bond was assumed at the interface of steel angles with concrete for specimens P–SC–T1-PB_ANG and P-MC-T1-PB_ANG, higher tensile strains were predicted in the bottom reinforcement of the beam at the face of the interior corbel (values were close to the yield strain). However, for the top reinforcement of the interior corbel at the face of the middle column, strains were significantly higher than the yield strain, as presented in Fig. 24(a) and (b) and Table 3.

Fig. 24(c) presents strain in the top reinforcement of the beam at the face of the interior column for the precast specimens with type (1) moment connections. Due to plastic hinge formation at the beam-column face, very high tensile strains of about 5.7 and 4.5 times the yield strain were predicted for specimens P-MC-T1-ANG and P-MC-T1-PB_ANG, respectively.

For precast specimens with type (1) moment connections, Fig. 24(d) and (e) show, respectively, strains in the top reinforcement of the beam at the faces of exterior corbel and column. As noted from the figures and Table 3, very high tensile strains were found for the top beam reinforcement at the face of the exterior corbel due to the formation of the plastic hinge at large displacement levels as explained earlier. However, as seen in Fig. 24(d) and (e), these strains are much higher than those predicted at the face of the exterior column. The reason is that the end of the precast beam was kept in touch with the outer corbel till the end of the analysis, thus increasing the effective beam depth at the column face, which, in turn, reduced the strain in the top reinforcement. Strains in the outer reinforcement of the exterior column close to the joint region are shown in Fig. 24(f). Due to discontinuity in the top beam reinforcement, small strains with values considerably less than the bar yield strain were predicted for the outer column bars of specimens with simple shear connections. However, for specimens with moment connections (P-MC-T1-ANG and P-MC-T1-PB_ANG), higher strains were predicted in the outer bars of the exterior columns. As seen in Table 3, these values were about 99% and 141% of the yield strain for specimens P-MC-T1-ANG and P-MC-T1-PB_ANG, respectively.

5.3.2. Precast specimens with type 2 connections

For precast specimens with type 2 connections, strains in the bottom beam reinforcement at the interior corbel face are shown in Fig. 25(a). As seen in Table 3 and Fig. 25(a), for all specimens, very small strains

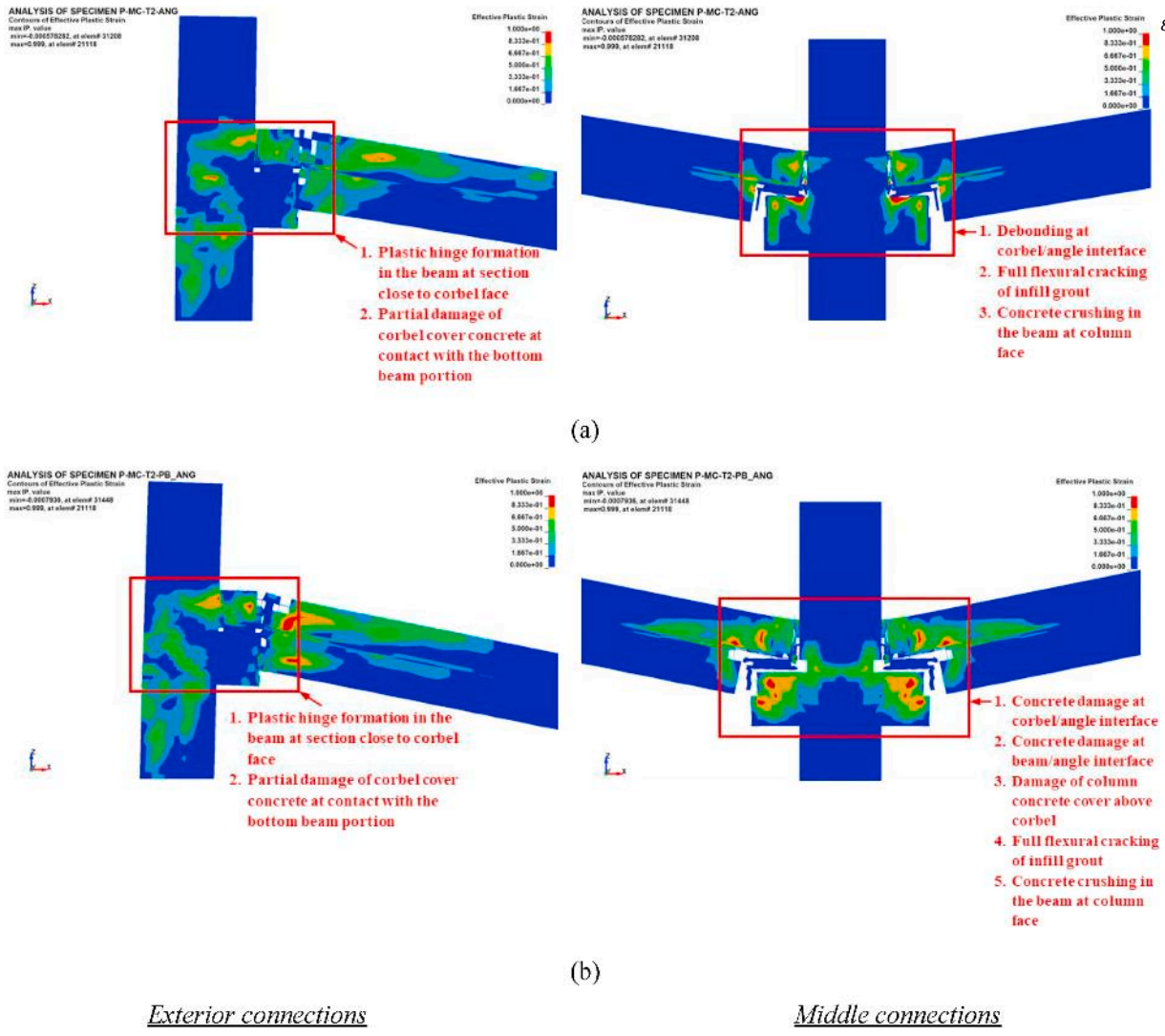

Fig. 21. Damage contours for: (a) P-MC-T2-ANG; (b) P-MC-T2-PB_ANG.

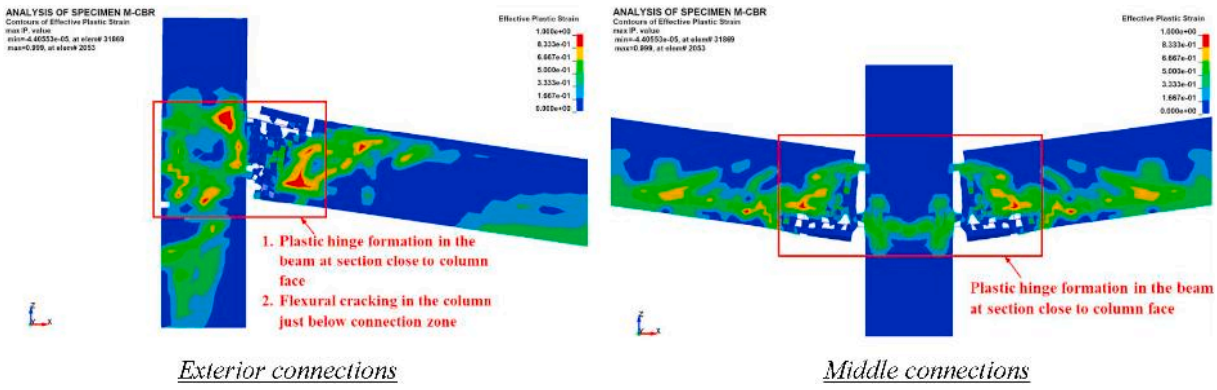

Fig. 22. Damage contours for monolithic assembly M-CBR.

(with values considerably less than the yield strain) were predicted owing to the cutoff of bottom beam reinforcement at the face of the inner corbel. Fig. 25(b) presents tensile strain in the top reinforcement of the interior corbel at the face of the middle column. Owing to debonding at the interface of steel angle with corbel, tensile strains in the top corbel reinforcement were less than the yield strain for specimens P–SC–T2-ANG and P-MC-T2-ANG. For specimen P–SC–T2-PB_ANG, although a perfect bond was assumed at the angle/corbel interface, the yield was not reached for the top reinforcement of the interior corbel, as shown in Table 3 and Fig. 25(b). The reason is that the load capacity of this assembly (= 26 kN transmitted per corbel) was small to induce yielding in the top corbel reinforcement. Nevertheless, for assembly P-MC-T2-PB_ANG, the load transmitted per corbel was 55 kN that was sufficient to induce yielding in the top corbel reinforcement, as seen from Fig. 25(b)

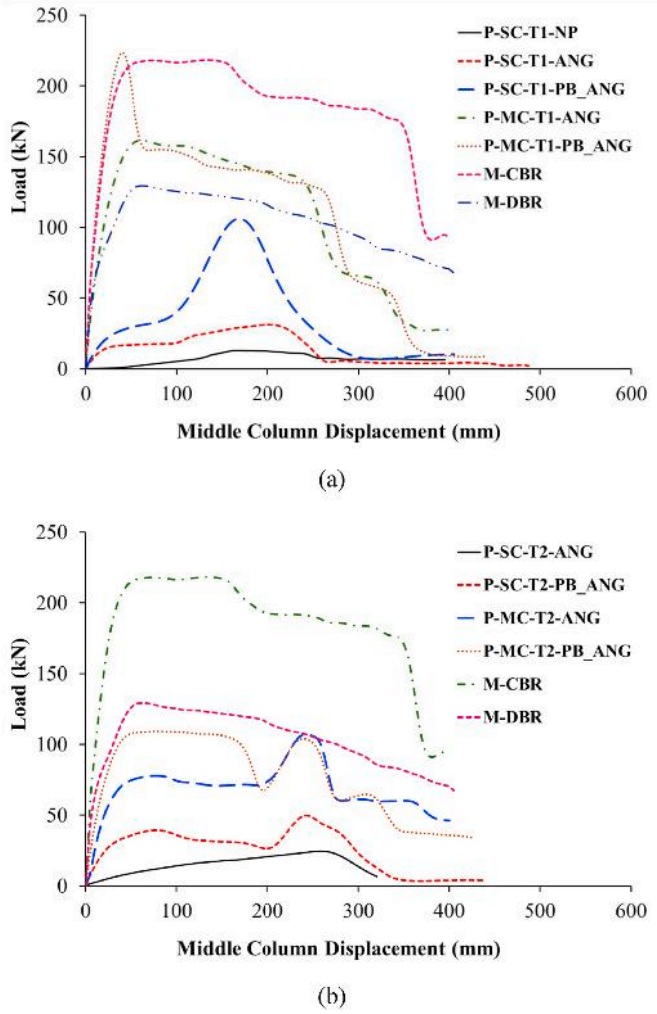

Fig. 23. Load versus displacement envelopes for precast assemblies with connections of: (a) Type (1); (b) Type (2).

and Table 3.

Fig. 25(c) presents strain in the top beam reinforcement at the face of the interior column for the precast specimens with type (2) moment connections. Due to plastic hinge formation at the beam-column interface, very high tensile strains of about 8.2 and 9 times the yield strain were predicted for specimens P-MC-T2-ANG and P-MC-T2-PB_ANG, respectively (see Table 3 and Fig. 25(c)).

For precast specimens with type (2) moment connections, Fig. 25(d) and (e) show strains in the top beam reinforcement at faces of exterior corbel and column, respectively. Very high tensile strains were obtained for the top beam reinforcement at the face of the outer corbel due to the development of the plastic hinge in the reduced beam section as discussed earlier. Nevertheless, as seen in Fig. 25(d) and (e), much smaller strains were predicted at the face of the exterior column. The reason is that the dapped end of the precast beam was kept in touch with the outer corbel till the analysis end (see Fig. 21), thus increasing the effective beam depth at the column face, which reduced the strain in the top reinforcement.

Fig. 25(f) displays strains in the outer reinforcement of the exterior column close to the joint region. Because of discontinuity in top beam reinforcement, small strains with values considerably less than the bar yield strain were predicted for outer column bars of specimens with simple shear connections. However, for specimens with moment connections (P-MC-T2-ANG and P-MC-T2-PB_ANG), higher strains were predicted in the outer bars of exterior columns. As seen in Table 3, these values were about 91% and 94% of the yield strain for specimens P-MC-T2-ANG and P-MC-T2-PB_ANG, respectively.

5.3.3. Monolithic specimens

Fig. 26(a)–(c) present the numerically predicted strains in steel bars at different locations of monolithic specimens M-CBR and M-DBR. It is clear from Fig. 26(a) and Table 3 that very high tensile strains (≈39 times the yield strain) were developed in the bottom beam reinforcement at the face of the interior column of specimen M-CBR. This is attributed to the continuity of the bottom reinforcement at the middle joint and hence the formation of plastic hinges in beams near the middle connection zone, as identified earlier. However, for specimen M-DBR, peak strain in the bottom beam reinforcement at the middle column face was about 95% of the yield strain. This was owing to the discontinuity of the bottom reinforcement in specimen M-DBR, which resulted in considerable slippage at the column interface as clarified previously in Fig. 17(c). Nevertheless, due to continuity of the top bars of the beams at the face of exterior columns in specimens M-CBR and M-DBR (and hence the formation of plastic hinges), very high tensile strains were predicted as identified in Fig. 26(b) and Table 3. These values were about 5.0 and 9.6 times the yield strain for specimens M-CBR and M-DBR, respectively. Fig. 26(c) shows strains in the outer reinforcement of the exterior column close to the joint region for monolithic specimens. Owing to continuity in the top beam reinforcement, very high strains were obtained for outer column reinforcement of specimens M-CBR and M-DBR. As seen in Table 3, these values were about 6.6 and 7.4 times the yield strain for specimens M-CBR and M-DBR, respectively.

5.4. Comparison of different connections

For comparing the behavior of studied precast connections in the event of middle column loss, three assessment parameters were developed in the current research. These are the maximum load, energy, and displacement efficiencies (α_P, α_E, and α_Δ), which are assessed from

$$\alpha_P = \frac{P_{u,pc}}{P_{u,m}} \times 100\% \tag{7}$$

$$\alpha_E = \frac{E_{pc}}{E_m} \times 100\% \tag{8}$$

$$\alpha_\Delta = \frac{\Delta_{u,pc}}{\Delta_{u,m}} \times 100\% \tag{9}$$

In the above equations, $P_{u,pc}$, E_{pc}, and $\Delta_{u,pc}$ are, respectively, the maximum load, dissipated energy, and ultimate displacement of the precast assembly; and $P_{u,m}$, E_m, and $\Delta_{u,m}$ are, in turn, the maximum load, dissipated energy, and ultimate displacement of its counterpart monolithic assembly having continuity in beam reinforcement (assembly M-CBR). It should be noted that the ultimate displacement of the assembly is taken as the displacement of the middle column at ultimate state, which is considered as the post-peak state when the drop in load reaches 20% of the maximum load [50]. The three parameters (α_P, α_E, and α_Δ) were assessed for all 9 precast specimens and monolithic assembly M-DBR (having discontinuous bottom beam bars), and they were, respectively, plotted in Fig. 27(a)–(c). It is worth mentioning that the specimens are arranged in Fig. 27(a)–(c) in the order of increasing efficiency.

It is generally noted that owing to the dapped beam end with reduced section for precast assemblies with type (2) connections, their progressive collapse resistance (with regard to maximum load and energy efficiency) is significantly lower than their type (1) counterparts. However, regarding the ultimate displacement, type (2) connections have better performance than type (1) precast connections (see Fig. 27(c)). For each precast-connection type (T1 and T2), both peak load and energy efficiencies of assemblies having moment connections are significantly more than specimens with simple shear connections.

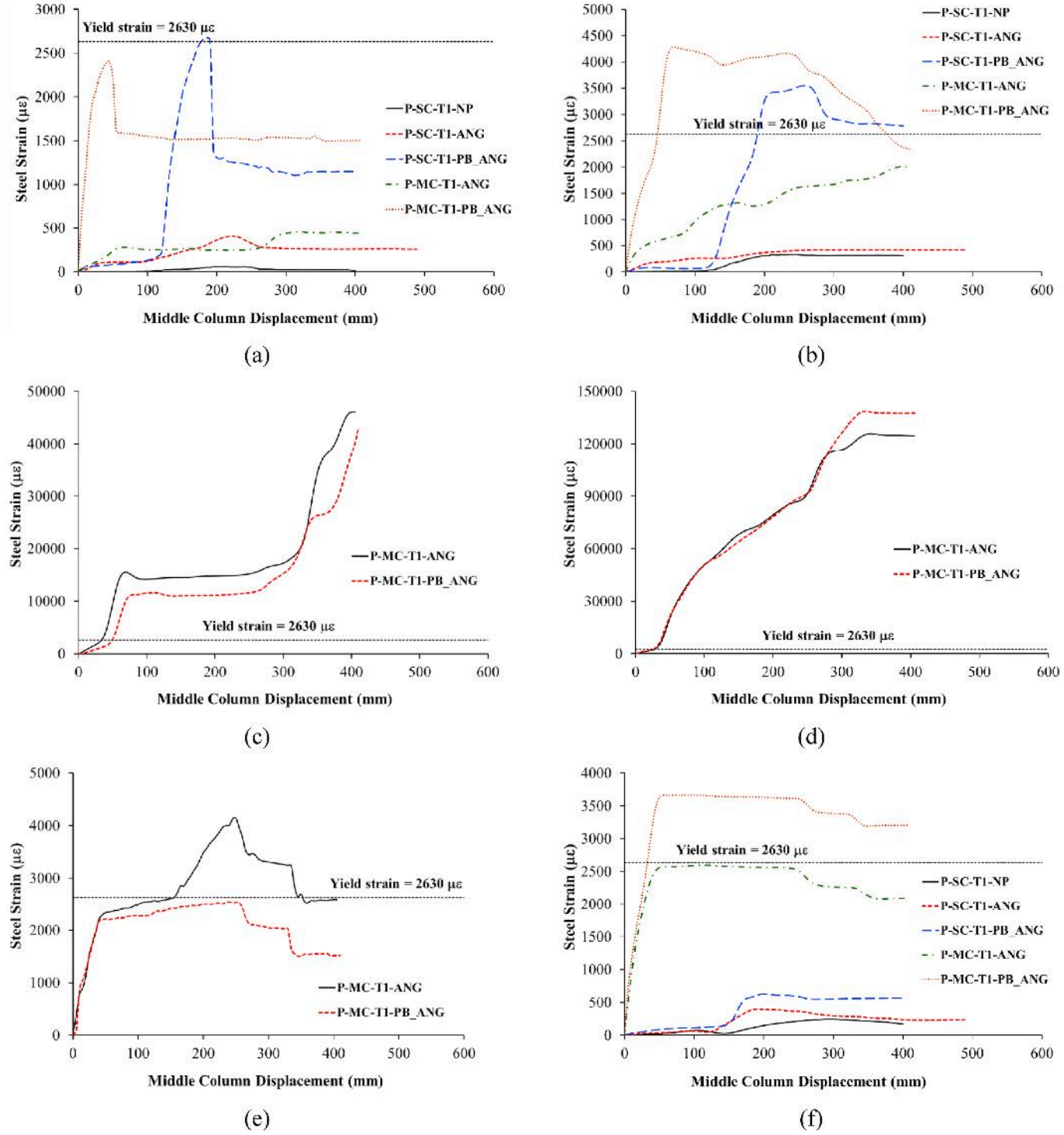

Fig. 24. Steel strain versus displacement plots for precast assemblies with type 1 connections: (a) Bottom steel of beam at middle corbel face; (b) Top steel of middle corbel at middle column face; (c) Top steel of beam at middle column face; (d) Top steel of beam at exterior corbel face; (e) Top steel of beam at exterior column face; (f) Outer steel of exterior column close to joint region.

Even though specimen P-MC-T1-PB_ANG had the highest load and energy efficiencies of 102% and 58%, in turn, it had the least displacement efficiency (= 16%). This is because it suddenly lost approximately 31% of its strength immediately after reaching the peak load (see Fig. 23 (a)). This behavior is brittle and highly undesirable. However, among all precast assemblies, specimen P–SC–T2-ANG had the highest displacement efficiency of 85% as seen in Fig. 27(c).

With respect to peak load and dissipated energy, the performance of precast specimens with T1 moment connections was better than the monolithic specimen M-DBR. Peak load efficiencies of T1 moment connections were 1.26 and 1.73 times that for monolithic specimen M-DBR. However, the energy efficiencies of T1 moment connections were 1.02 and 1.14 times that for monolithic assembly M-DBR. On the other hand, the peak load and energy efficiencies of precast specimens with T2 moment connections were less than monolithic specimen M-DBR by about 15%–17% and 27%–43%, respectively. Nevertheless, as seen in

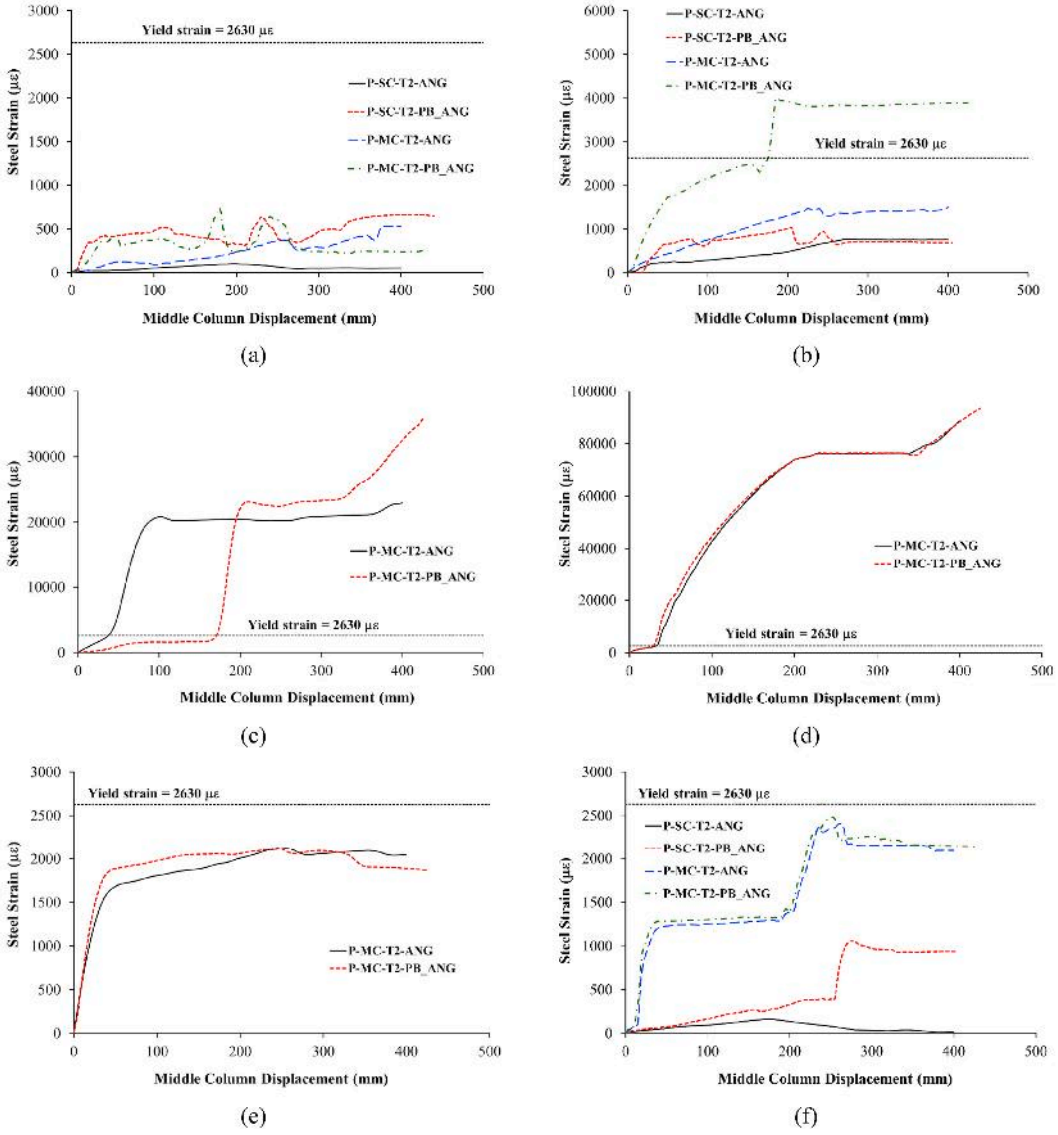

Fig. 25. Steel strain versus displacement plots for precast assemblies with type 2 connections: (a) Bottom steel of beam at middle corbel face; (b) Top steel of middle corbel at middle column face; (c) Top steel of beam at middle column face; (d) Top steel of beam at exterior corbel face; (e) Top steel of beam at exterior column face; (f) Outer steel of exterior column close to joint region.

Fig. 27(c), the displacement efficiency of all precast specimens was less than the monolithic assembly M-DBR by about 2%–82%.

The ultimate rotational ductility was calculated for both the precast moment-connection assemblies and monolithic specimen M-CBR from

$$\text{Ultimate rotational ductility} = \frac{\theta_u}{\theta_y} \tag{10}$$

where θ_u and θ_y are the beam chord rotation at the ultimate state and first yielding of reinforcement passing through the joint, respectively. As previously mentioned, the ultimate state is considered as the post-peak state that corresponds to a 20% drop in the maximum load. The beam end rotation is computed as $\theta = \tan^{-1}(\Delta/L)$, where Δ is the middle column displacement and L is the centerline-to-centerline beam span (= 3000 mm). Fig. 28 shows the ultimate rotational ductility for both the precast moment-connection specimens and monolithic assembly M-CBR. For purpose of comparison, the rotational ductility of the precast moment-connection specimens tested by Quiel et al. [34] was also added to Fig. 28. In comparison with the monolithic specimen M-CBR, it is generally identified that except for assembly P-MC-T1-PB_ANG that has limited ductility of 1.7, all numerically studied precast moment-connection specimens have moderate rotational ductility levels ranging from 7.0 to 9.3 (43%–57% of specimen M-CBR). It is found that precast specimens with T2 moment connections have higher rotational ductility than assemblies with T1 moment connections, and the highest ductility of 9.3 was provided by specimen P-MC-T2-PB_ANG. It is also clarified from Fig. 28 that the rotational ductility levels of the precast moment-connection specimens P-MC-T1-ANG, P-MC-T2-ANG, and P-MC-T2-PB_ANG are close to the moderate ductility level of specimen "Test 2" of Quiel et al. [34]. However, both precast moment-connection specimens P-MC-T1-PB_ANG and "Test 1" of Quiel et al. [34] have limited rotational ductility as demonstrated in Fig. 28.

6. Conclusions

In this study, 11 half-scale beam-column assemblies – comprising two beams and three columns – were numerically investigated under the middle column removal scenario using nonlinear 3D FE modeling. Two specimens represented typical existing precast simple beam-column connections, and three specimens had revised precast simple connections. Four assemblies were designed with new precast moment

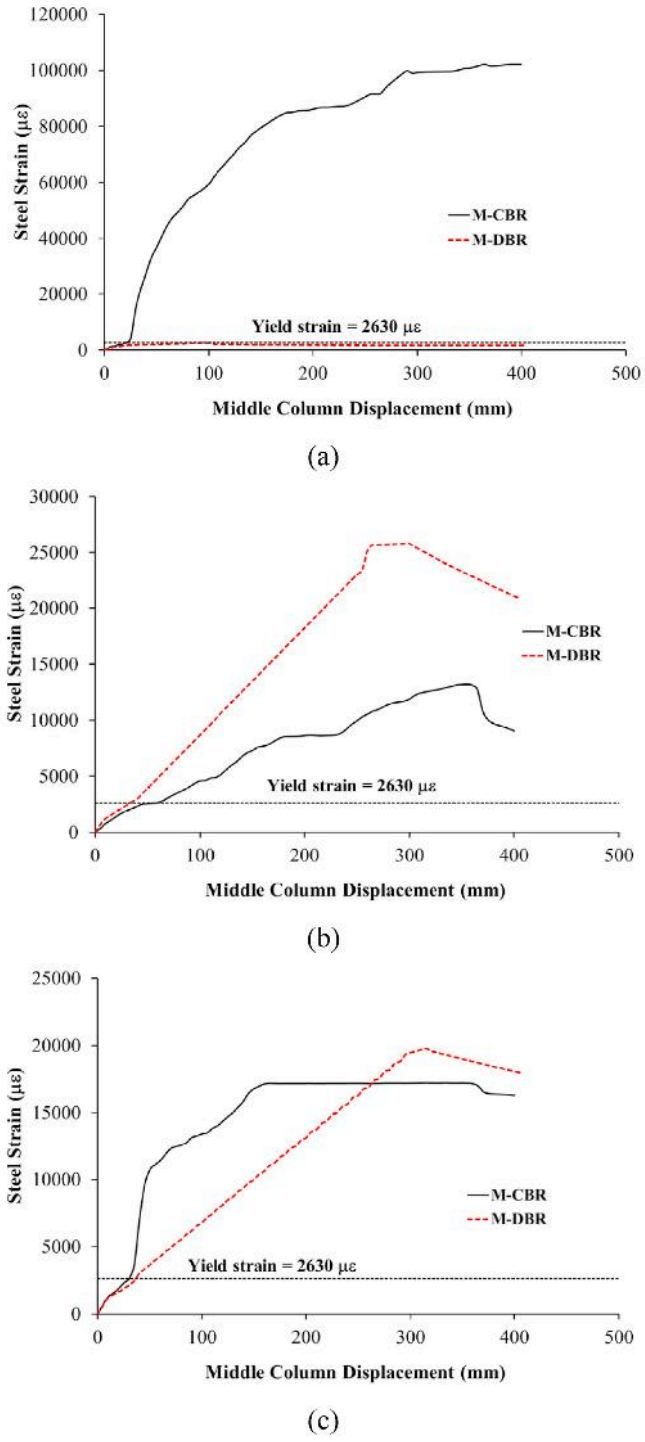

Fig. 26. Steel strain versus displacement plots for monolithic assemblies: (a) Bottom steel of beam at middle column face; (b) Top steel of beam at exterior column face; (c) Outer steel of exterior column close to joint region.

connections. The last two specimens represented monolithic concrete beam-column connections with continuous and discontinuous longitudinal beam bars to be compared with the precast assemblies. The performance of different assemblies was compared with regard to failure mode and load-displacement response. The prime conclusions of this research are as follows:

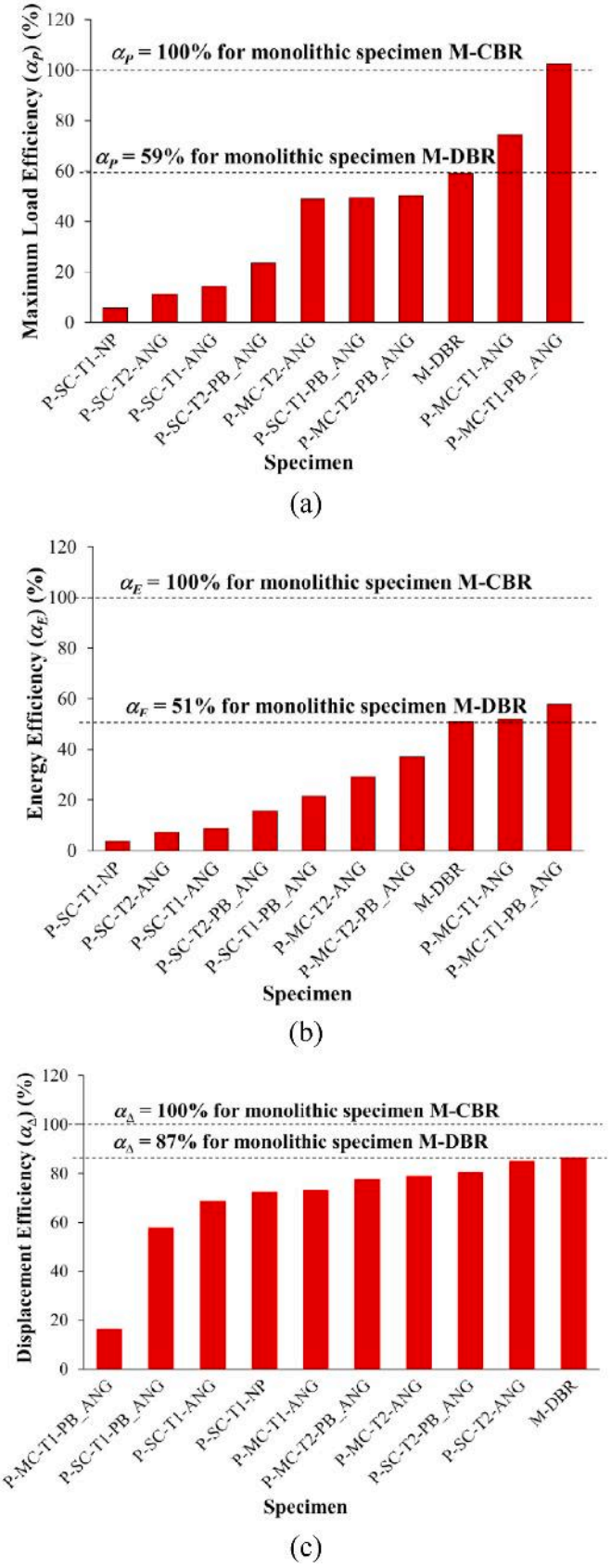

Fig. 27. Effect of detailing of beam-column connection on: (a) Maximum load efficiency; (b) Energy efficiency; (c) Displacement efficiency.

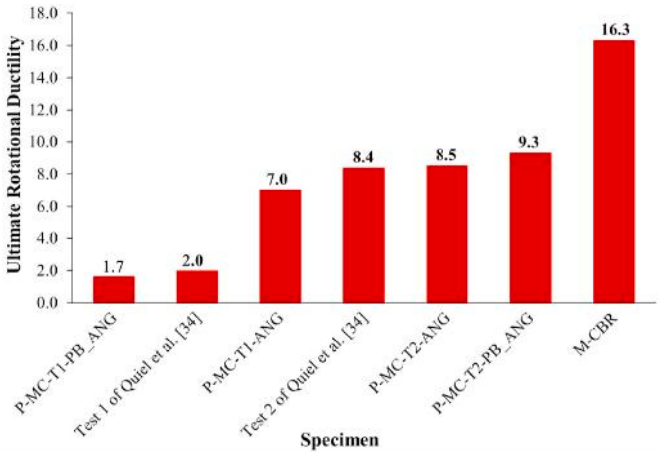

Fig. 28. Comparison between precast moment-connection specimens with respect to ultimate rotational ductility.

1. Precast RC frames with simple shear connections had low load-carrying capacity, and hence they are vulnerable to the risk of progressive collapse under column-loss events.
2. Compared with specimens with simple shear connections, precast moment-connection assemblies had higher load-carrying capacity and improved load-displacement response. The progressive collapse capacities of specimens with moment connections were considerably higher than their simple shear counterparts by about 107%–417% and 112%–338% for T1 and T2 specimens, respectively.
3. The predicted progressive collapse capacities (with regard to peak load and dissipated energy) of precast specimens with T1 moment connections were noticeably larger than their T2 counterparts. This is because of the dapped beam end with reduced section at the corbel face for T2 specimens. However, precast specimens with T2 moment connections had considerably higher ultimate displacement and rotational ductility than their T1 counterparts.
4. Among all investigated specimens with precast moment connections, specimen P-MC-T1-PB_ANG had the worst performance. This is because it suddenly lost approximately 31% of its strength immediately after reaching the peak load. This behavior is brittle and highly undesirable. However, specimen P-MC-T2-PB_ANG had the highest rotational ductility before a significant strength drop was observed. Therefore, this connection is recommended for diminishing the potential of progressive collapse in exterior precast RC frames of multistory buildings.
5. Progressive collapse resistance of studied specimens was compared based only on their behavior in the flexural action stage. This is because the catenary-action phase was not reached in either testing or analysis of control monolithic specimen M-CBR owing to the inadequate restraint given by exterior columns and the discontinuity of beams past the outer columns.
6. The FE models developed in this research were effective at assessing the progressive collapse potential of both precast and monolithic RC assemblies in the event of column loss. These models may be relied upon in upcoming studies on the progressive collapse potential of precast concrete assemblies with different connection designs.

CRediT authorship contribution statement

Hussein M. Elsanadedy: Conceptualization, Methodology, Visualization, Validation, Writing – original draft.

Declaration of competing interest

The authors declare that they have no known competing financial interests or personal relationships that could have appeared to influence the work reported in this paper.

Acknowledgements

The author is grateful to the Deanship of Scientific Research, King Saud University, for funding through Vice Deanship of Scientific Research Chairs.

References

[1] H.K. Choi, Y.C. Choi, C.S. Choi, Development and testing of precast concrete beam-to-column connections, Eng. Struct. 56 (2013) 1820–1835.
[2] R. Vidjeapriya, K.P. Jaya, Experimental study on two simple mechanical precast beam column connections under reverse cyclic loading, J. Perform. Constr. Facil. 27 (2013) 402–414.
[3] R. Vidjeapriya, K.P. Jaya, Behaviour of precast beam-column mechanical connections under cyclic loading, Asian J. Civil Eng. (Build Hous) 13 (2014) 233–245.
[4] O. Ertas, S. Ozden, T. Ozturan, Ductile connections in precast concrete moment resisting frames, PCI J. 5 (2006) 2–12.
[5] M.K. Joshi, C.V. Murty, M.P. Jaisingh, Cyclic behaviour of precast RC connections, Indian Concr. J. 79 (2005) 43–50.
[6] A. Kheyroddin, H. Dabiri, Cyclic performance of RC beam-column joints with mechanical or forging (GPW) splices; an experimental study, Structure 28 (2020) 2562–2571.
[7] H. Dabiri, A. Kaviani, A. Kheyroddin, Influence of reinforcement on the performance of non-seismically detailed RC beam-column joints, J. Build. Eng. 31 (2020) 101333.
[8] R.A. Hawileh, A. Rahman, H. Tabatabai, Nonlinear finite element analysis and modeling of a precast hybrid beam-column connection subjected to cyclic loads, Appl. Math. Model. 34 (2010) 2562–2583.
[9] G.S. Cheok, W.C. Stone, Performance of 1/3 Scale Model Precast Concrete Beam–Column Connections Subjected to Cyclic Inelastic Loads, NIST, Gaithersburg, MD, 1994. Report No. NISTIR 5436.
[10] M. Kaya, A.S. Arslan, Analytical modeling of post-tensioned precast beam-to-column connections, Mater. Des. 30 (2009) 3802–3811.
[11] X. Cai, Z. Pan, Y. Zhu, N. Gong, Y. Wang, Experimental and numerical investigations of self-centering post-tensioned precast beam-to-column connections with steel top and seat angles, Eng. Struct. 226 (2021) 111397.
[12] K. Ding, Y. Ye, W. Ma, Seismic performance of precast concrete beam-column joint based on the bolt connection, Eng. Struct. 232 (2021) 111884.
[13] J.H. Hwang, S.H. Choi, D.H. Lee, K.S. Kim, O.S. Kwon, Seismic behaviour of post-tensioned precast concrete beam–column connections, Mag. Concr. Res. 73 (9) (2021) 433–447.
[14] D.E. Allen, W.R. Schriever, Progressive Collapse, Abnormal Load, and Building Codes, Structural Failure: Modes, Causes, Responsibilities, Proc. American Society of Civil Engineers, New York, USA, 1972.
[15] T.H. Almusallam, H.M. Elsanadedy, H. Abbas, S.H. Alsayed, Y.A. Al-Salloum, Progressive collapse analysis of a RC building subjected to blast loads, Int. J. Struct. Eng. Mech. 36 (3) (2010) 301–319.
[16] H.M. Elsanadedy, T.H. Almusallam, Y.R. Alharbi, Y.A. Al-Salloum, H. Abbas, Progressive collapse potential of a typical steel building due to blast attacks, J. Constr. Steel Res. 101 (2014) 143–157.
[17] S.M. Baldridge, F.K. Humay, Reinforced Concrete and Secure Buildings: Progressive Collapse, in: The Structural Bulletin Series, vol. 2, Concrete Reinforcing Steel Institute, 2004.
[18] J. Choi, D. Chang, Prevention of progressive collapse for building structures to member disappearance by accidental actions, J. Loss Prevent. Proc. 22 (2009) 1016–1019.
[19] Y.A. Al-Salloum, T.H. Almusallam, M.Y. Khawaji, T. Ngo, H.M. Elsanadedy, H. Abbas, Progressive collapse analysis of RC buildings against internal blast, Adv. Struct. Eng. 18 (12) (2015) 2181–2192.
[20] P.X. Dat, T.K. Haiand, Y. Jun, A simplified approach to assess progressive collapse resistance of reinforced concrete framed structures, Eng. Struct. 101 (2015) 45–57.
[21] Y. Bao, S.K. Kunnath, S. El-Tawil, H.S. Lew, Macromodel-based simulation of progressive collapse: RC frame structures, J. Struct. Eng-ASCE 134 (7) (2008) 1079–1091.
[22] I. Azim, J. Yang, S. Bhatta, F. Wang, Q-f. Liu, Factors influencing the progressive collapse resistance of RC frame structures, J. Build. Eng. 27 (2020) 100986.
[23] Y.-H. Weng, K. Qian, F. Fu, Q. Fang, Numerical investigation on load redistribution capacity of flat slab substructures to resist progressive collapse, J. Build. Eng. 29 (2020) 101109.
[24] H.M. Elsanadedy, Y.A. Al-Salloum, M.A. Alrubaidi, T.H. Almusallam, H. Abbas, Finite element analysis for progressive collapse potential of precast concrete beam-to-column connections strengthened with steel plates, J. Build. Eng. (2020) 101875.
[25] M. Sasani, M. Bazan, S. Sagiroglu, Experimental and analytical progressive collapse evaluation of actual reinforced concrete structure, ACI Struct. J. 104 (6) (2007) 731–739.
[26] J. Yu, K. Tan, Experimental and numerical investigation on progressive collapse resistance of reinforced concrete beam column sub-assemblages, Eng. Struct. 55 (2013) 90–106.

[27] M. Li, M. Sasani, Integrity and progressive collapse resistance of RC structures with ordinary and special moment frames, Eng. Struct. 95 (2015) 71–79.
[28] T. Wang, Q. Chen, H. Zhao, L. Zhang, Experimental study on progressive collapse performance of frame with specially shaped columns subjected to middle column removal, Shock Vib. (2016) 13. Article ID 7956189.
[29] S.B. Kang, K.H. Tan, Behaviour of precast concrete beam-column sub-assemblages subject to column removal, Eng. Struct. 93 (2015) 85–96.
[30] S.B. Kang, K.H. Tan, E. Yang, Progressive collapse resistance of precast beam-column sub-assemblages with engineered cementitious composites, Eng. Struct. 98 (2015) 186–200.
[31] R.B. Nimse, D.D. Joshi, P.V. Patel, Behavior of wet precast beam column connections under progressive collapse scenario: an experimental study, Int. J. Adv. Struct. Eng. 6 (2014) 149–159.
[32] D.J. Morone, H. Sezen, Simplified collapse analysis using data from building experiment, ACI Struct. J. 111 (4) (2014) 925–934.
[33] J.A. Main, Y. Bao, H.S. Lew, F. Sadek, V.P. Chiarito, S.D. Robert, J.O. Torres, An Experimental and Computational Study of Precast Concrete Moment Frames under a Column Removal Scenario, National Institute of Standards and Technology, Gaithersburg, MD, 2015, https://doi.org/10.6028/NIST.TN.1886.
[34] S.E. Quiel, C.J. Naito, C.T. Fallon, A non-emulative moment connection for progressive collapse resistance in precast concrete building frames, Eng. Struct. 179 (2019) 174–188.
[35] Y. Zhou, X. Hu, Y. Pei, H.J. Hwang, T. Chen, W. Yi, L. Deng, Dynamic load test on progressive collapse resistance of fully assembled precast concrete frame structures, Eng. Struct. 214 (2020) 110675.
[36] T.H. Almusallam, H.M. Elsanadedy, Y.A. Al-Salloum, N.A. Siddiqui, R.A. Iqbal, Experimental investigation on vulnerability of precast RC beam-column joints to progressive collapse, KSCE J. Civ. Eng. 22 (10) (2018) 3995–4010.
[37] M.A. Alrubaidi, Rehabilitation of Beam-Column Connections in Existing Precast Concrete Buildings for Progressive Collapse Mitigation, King Saud University, 2016. MS Thesis.
[38] H.M. Elsanadedy, T.H. Almusallam, Y.A. Al-Salloum, H. Abbas, Investigation of precast RC beam-column assemblies under column-loss scenario, Construct. Build. Mater. 142 (2017) 552–571.
[39] Aci Committee 318, Building Code Requirements for Structural Concrete and Commentary, vols. 318–19, American Concrete Institute, Detroit, MI, USA, 2019. ACI.
[40] Livermore Software Technology Corporation, LS-DYNA Keyword User's Manual –, vols. 1–3, LSTC, Livermore, CA, 2018. Version R11.
[41] T.B. Belytschko, C.S. Tsay, Explicit algorithms for non-linear dynamics of shells, J. Appl. Mech. Applied Mechanics Division, ASME 48 (1981) 209–231.
[42] Y.D. Murray, A. Abu-Odeh, R. Bligh, Evaluation of Concrete Material Model 159, US Department of Transportation, Federal Highway Administration National Transportation Systems Center, USA, 2007. Report No. FHWA-HRT-05-063.
[43] R.M. Christensen, A nonlinear theory of viscoelasticity for application to elastomers, J. Appl. Mech. Applied Mechanics Division, ASME 47 (1980) 762–768.
[44] H.M. Elsanadedy, T.H. Almusallam, S.H. Alsayed, Y.A. Al-Salloum, Flexural strengthening of RC beams using textile reinforced mortar – experimental and numerical study, Compos. Struct. 97 (2013) 40–55.
[45] California Department of Transportation, Memo to Designers 7-1 (Bridge Bearings), June 1994, p. 69p.
[46] Y. Xiao, M. Rui, Seismic retrofit of RC circular columns using prefabricated composite jacketing, J. Struct. Eng. ASCE 123 (10) (1997) 1357–1364.
[47] ACI Committee 408, Bond and Development of Straight Reinforcing Bars in Tension, ACI 408R-03, American Concrete Institute, Detroit, MI, USA, 2003.
[48] H.M. Elsanadedy, Y.A. Al-Salloum, T.H. Almusallam, T. Ngo, H. Abbas, Assessment of progressive collapse potential of special moment resisting RC frames–Experimental and FE study, Eng. Fail. Anal. 105 (2019) 896–918.
[49] R. Tepfers, P. Olsson, Ring test for evaluation of bond properties of reinforcing bars. Int. Conf. On Bond in Concrete from Research to Practice, Riga, Latvia, 1992, pp. 189–199.
[50] NZS 4203, New Zealand Standard (NZS), Code of Practice for General Structural Design and Design Loadings for Buildings 1, 1992. New Zealand.